FY 2017-2018, Final Report
Project name: Understanding Water Controls on Shale Gas/Oil Mobilization into Fractures

Contract: ESD14085
Tetsu Tokunaga, Jiamin Wan, Abdullah Cihan, Yingqi Zhang, Stefan Finsterle, Ken Tokunaga

Reporting period: October 1, 2016 to September 30, 2018

Executive Summary:
The overall objective of this research is to understand and predict the dynamics of hydraulic fracturing fluid interactions within unconventional shale reservoirs, focusing on the controlling roles of water at and around zones of fractures and adjacent shale matrix. To address this objective, we have conducted laboratory tests and modeling studies on water interactions with shales. Understanding gained from these activities is intended to strengthen the scientific basis for designing more effective hydraulic fracturing strategies that may ultimately maximize gas production while utilizing significantly less water [*Gupta,* 2009; *Montgomery,* 2013]. This Final Report summarizes work directed toward two general objectives. The first is to understand the coupling between water (or alternative fracturing fluids) uptake and gas counter flow (counter-current imbibition) in shales in order to help identify approaches to improving production. Under this first objective, we examined consequences of immiscible fluid displacement at fracture-shale matrix interfaces, within shale matrix blocks, and at larger scales of matrix blocks transected by fracture networks where influences of gravity drainage are potentially important (Figure 1). Understanding of the energetics of water interactions with shales and rates of water imbibition/drainage from shales is essential developing more mechanistic foundations for improving water use in hydraulic fracturing. The second general objective is to understand the influence of non-water fracturing fluids on shale gas/oil mobilization, and to identify the optimal formulas of fracturing fluids for specific oil types and reservoir wettability. In order to achieve these objectives, new experimental and modeling approaches were initiated.

Activities completed though this study include

(1) A set of physicochemical analyses of Woodford and Mahantango/Marcellus Shales were completed. These consisted of elemental and mineralogical analyses, and measurements bulk density, grain density, and porosity.

(2) Water absorption-imbibition and drainage-desorption relations were measured in shales over wide ranges in capillary pressure and relative humidity [*Tokunaga et al.*, 2017].

(3) Experiments that measured rates of vapor diffusion in Mahantango and Marcellus Shale sidewall cores were conducted under a relative humidity (rh) of 0.31 and 0.81 (50 ˚C). At the rh of 0.31, measurements were obtained for diffusion parallel and perpendicular to bedding planes.

(4) Experiments and modeling of the influence of adsorbed water on methane adsorption in shales from the Qaidam Basin were performed in our LBNL laboratory in collaboration with the China University of Geosciences (Beijing). Much of that work was summarized in a recent publication [*Wang et al.*, 2018].

(5) Tests of novel natural biosurfactants to stabilize CO_2 foams at elevated pressures and temperatures were completed, and results recently published [*Wan et al.*, 2017].

(6) Development of a high-pressure micromodel system for pore-scale visualization of fracture-matrix interactions.

(7) Construction of a new, closed-loop, high pressure foam generator was completed, and tests of CO_2 foams were conducted.

(8) Modeled water vapor diffusion into shales, without and with anisotropic effective diffusion coefficients.

(9) Continued development of a new theoretical model for representing water imbibition and distribution in shale matrix and matrix-fracture interfaces.

(10) Modeled laboratory-measured water imbibition rates into shales.

(11) Modeled the dynamics of fracture fluid redistribution and gas flow at the scale of single hydraulic fractures.

(12) Modeled CO_2 as an alternative fracking fluid, comparing its performance relative to previous simulations with slickwater under otherwise identical conditions.

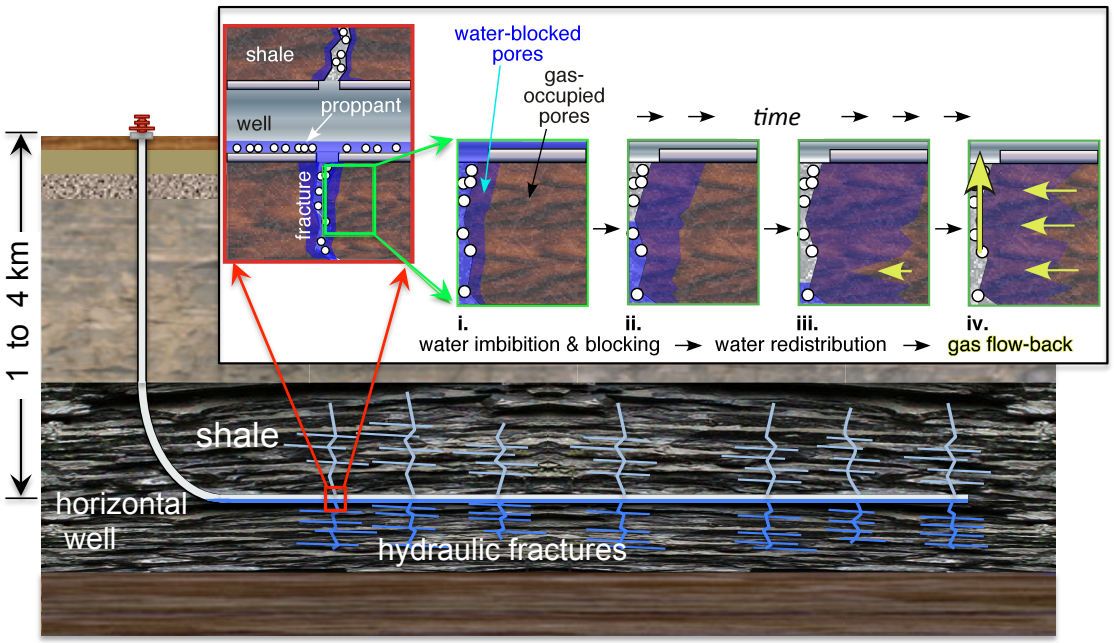

Figure 1. Conceptual illustration of hydraulic fractures generated from horizontal wells in a shale gas reservoir. Fractures residing above the horizontal well are hypothesized to drain quickly, thus are only weakly affected by water blocking and facilitate early gas production. Fractures residing below the horizontal well are hypothesized to drain slowly, such that gas production becomes possible as the water level declines in the fracture, primarily through imbibition into the shale matrix. The insert depicts the time-dependent localized distribution of injected water along fracture-shale matrix interfaces following hydraulic fracturing, along with declining water level in a fracture below the horizontal well. Note that counter-flow (counter-current imbibition) of gas to the well through redistribution of imbibed water is hypothesized to be significant only in regions adjacent to drained portions of fractures.

Work Performed:

Task 1. Basic characterization of shale properties

Shale Samples: Woodford Shale samples have been our primary test materials because of its importance as a major gas and oil source rock [*Cardott*, 2012] and because of earlier availability. Samples from five different locations within this formation were obtained from the Oklahoma Geological Survey (http://www.ogs.ou.edu/level3-OPICcorefacility.php) at the beginning of the first phase of this project. The table from our previous annual report is included here to provide background characteristics of these materials (Table 1). More recently (September 2016), we received a set of Marcellus and Mahantango Shales sidewall cores from the MSEEL, and these are being prepared for a variety of tests including adsorption-desorption isotherms, permeabilities, and imbibition rates. The samples received from MSEEL are listed in Table 2, and photographs of several prepared cores are shown in Figure 2.

sample source, origin

LBNL#	OGS#	well	sample depth, m	county
WHf	956	Hoffman	4346.3 - 4347.2	Custer, OK
WR	482	Roetzal	2569.0 - 2569.9	Blaine, OK
WD	4599	Dunkin	282.3 - 283.1	Wagoner, OK
WH1	2595	Holt	1126.7 - 1127.6	Okfuskee, OK
WH2	2595	Holt	1128.5 - 1129.4	Okfuskee, OK

major elements, carbon (organic and inorganic) contents, and major minerals

LBNL#	Al, %	Si, %	P, %	S, %	K, %	Ca, %	Ti, %	Mn, %	Fe, %	Total Carbon %	Inorganic Carbon %	Organic Carbon %	major minerals
WHf	9.1	22.2	0.1	0.3	3.5	1.2	0.4	0.09	3.1	4.3	0.40	3.9	q, il
WR	6.6	32.5	0.1	0.9	3.3	1.0	0.3	0.04	2.0	7.1	0.00	7.1	q, il
WD	8.6	30.0	0.1	0.3	4.3	1.3	0.3	0.03	3.0	6.1	0.46	5.6	q, il
WH1	4.8	22.0	0.1	0.1	1.8	11.7	0.2	0.01	1.0	6.3	3.6	2.7	q, il, c
WH2	10.0	37.6	0.2	0.2	5.2	2.4	0.5	0.02	2.1	5.5	0.00	5.5	q, il

q = quartz, il = illite, c = calcite

densities and porosities (provisional)

LBNL#	well	bulk density g/cm3	grain density g/cm3	porosity
WHf	Hoffman	2.58	2.76	0.065
WR	Roetzal	2.41	2.62	0.081
WD	Dunkin	2.41	2.59	0.070
WH1	Holt	2.42	2.69	0.100
WH2	Holt	2.50	2.68	0.067

specific surface areas

LBNL#	BET (N2) m2/g	BET (Kr) m2/g	BET (H2O m2/g	BET (H2O 50˚C) m2/g	GAB (H2O m2/g	GAB (H2O m2/g
WHf	0.21	0.27	13.5	17.5	11.6	13.4
WR	0.24	0.29	15.6	18.4	11.7	13.2
WD	0.31		13.5	15.0	13.6	12.8
WH1	3.03		8.5	8.7	7.3	7.2
WH2	0.91		15.2	17.1	12.7	13.1

Table 1. Woodford shale samples included in experimental parts of this project, identified by LBNL label, Oklahoma Geological Survey (OGS) number, well depth, and county. LBNL-measured properties. All of these shales are being used for determining water vapor adsorption-desorption isotherms. The WR, WD, and WH1 shales are also being used to quantify vapor diffusion rate controls on adsorption equilibration times.

SW Depth	depth,	Sample ID	Complete ID	Formation
ft	m			
7221	2201.0	126-7221	4-126-M22-7221	Mahantango Shale
7271	2216.2	122-7271	4-122-M18-7271	Mahantango Shale
7326	2233.0	118-7326	4-118-M14-7326	Mahantango Shale
7391	2252.8	112-7391	4-112-M8-7391	Mahantango Shale
7426	2263.4	89-7426	3-89-M23-7426	Marcellus Shale
7430	2264.7	85-7430	3-85-M19-7430	Marcellus Shale
7444	2268.9	73-7444	3-73-M7-7444	Marcellus Shale
7447	2269.8	70-7447	3-70-M4-7447	Marcellus Shale
7463	2274.7	51-7463	2-51-M11-7463	Marcellus Shale
7470	2276.9	43-7470	2-43-M3-7470	Marcellus Shale

Table 2. Marcellus and Mahantango Shale sidewall cores received from MSEEL-NETL.

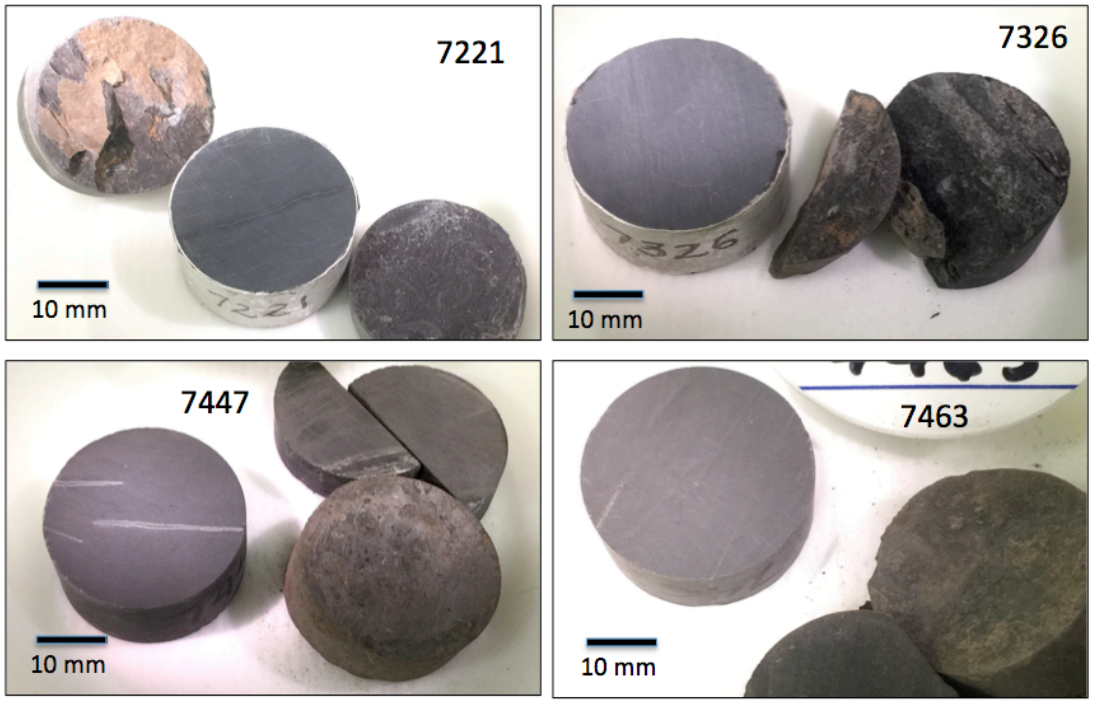

Figure 2. Several of the Marcellus sidewall core samples received from MSEEL-NETL, being prepared for testing (numbers are depth below ground surface, ft). Note visible bedding plane lamination across all cut surfaces.

Given the laminated structure of shales, their effective diffusion coefficients and permeabilities are expected to be strongly directionally-dependent (anisotropic), favoring transport parallel to the bedding plane. Such anisotropy is expected to facilitate gas flow horizontally to vertical hydraulic fractures, while vertical flow across unfractured laminae is expected to be more restricted. Thus, measurements of the directional dependence of transport properties are needed to quantify the importance of anisotropy, and to provide input for larger scale modeling. Given the fairly generic

nature of diffusive transport, these measurements are useful for quantifying anisotropy effects on both water vapor and natural gas.

Sidewall cores were received from the Marcellus Shale Energy and Environmental Laboratory (MSEEL) Science Well. For examination of anisotropy in effective diffusion coefficients, intact samples of sufficient size are needed. Of the ten specimens received from MSEEL, six core plugs had lengths greater than 1 cm and were selected for the diffusion studies. Specifically, samples 7271, 7391, 7426, 7430, 7444 and 7470 were selected (numbers identify sampling depth in feet, within the Science Well). The shallower 7271 and 7391 samples are from the Mahantango Shale, while the remaining four samples are from the deeper Marcellus Shale. Elemental compositions of these shales were obtained with X-ray fluorescence analyses (ALS USA, Inc.). Analytical results reported previously are presented in Table 3. As noted in a previous report, the 7426' specimen exhibited anomalously high uptake of water at $rh = 0.81$, expansion and splitting of the core plug (breaking of the epoxy-fixed Al foil sleeve), as well as net mass increase (even after oven-drying).

	Al	Si	Fe	K	Ca	Mg	Na	Ti	Ba	Sr	Mn	Cr	S	P	total C	organic C	inorganic C
	%	%	%	%	%	%	%	%	%	%	%	%	%	%	%	%	%
Mahantango, 7271'	10.63	26.80	4.56	3.75	0.25	1.07	0.45	0.46	0.32	0.025	0.023	0.014	1.50	0.039	1.73	1.66	0.07
Mahantango, 7391'	8.59	27.45	5.22	3.06	0.88	0.88	0.34	0.38	0.10	0.017	0.015	0.007	2.34	0.039	2.50	2.36	0.14
Marcellus, 7426'	9.29	23.45	5.50	3.46	2.17	0.82	0.36	0.37	0.30	0.025	0.015	0.007	2.66	0.039	4.67	4.24	0.43
Marcellus, 7430'	10.03	26.65	4.31	3.69	0.43	0.81	0.42	0.46	0.13	0.017	0.015	0.007	2.24	0.031	2.77	2.70	0.07
Marcellus, 7444'	9.10	26.35	3.85	3.44	1.11	0.91	0.42	0.40	0.13	0.017	0.015	0.007	1.41	0.026	4.87	4.57	0.30
Marcellus, 7470'	8.38	26.59	3.39	3.15	1.07	0.87	0.50	0.43	0.13	0.025	0.015	0.014	1.26	0.044	7.01	6.60	0.41
ALS Global, Reno, NV																	

Table 3. Major element composition of Mahantango and Marcellus Shales determined by X-ray fluorescence spectrometry.

Based on the high Ca and S concentrations of the 7426' sample, we initially considered the possibility that it contained anhydrite, $CaSO_4$, and that transformation to gypsum ($CaSO_4 \bullet 2H_2O$) under the elevated rh [*Freyer and Voigt*, 2003], thereby resulting in increased bulk volume. However, X-ray diffraction (XRD, Table 4) results indicate lack of significant concentrations of either anhydrite or gypsum, thus do not support that hypothesized mechanism for swelling. Furthermore, the XRD results showed that smectite is practically absent in all of our samples, thus swelling attributable to hydration-induced expansion of 2:1 clays is probably minor.

The XRD results of the 7426' sample showed that it contained an unusually high amount of pyrite (10%), a dense Fe(II) mineral susceptible to oxidation under oxygenated and humid conditions. The high pyrite content of this sample is consistent with the observed expansion and splitting of the core after exposure to elevated relative humidity (described in Task 2.A.3). Prior to drilling and sampling, the shales were certainly under reducing conditions. As receive, the samples were relatively dry, and further oven-dried prior to beginning the diffusion/adsorption experiments. Previous studies have shown that pyrite oxidation in air is slow, but accelerated at high relative humidities [*Borek*, 1994; *Huggins et al.*, 1983; *Jerz and Rimstidt*, 2004], and that this causes swelling of the host rock [*Hoover et al.*, 2015].

	Illite+Mica	Quartz	Pyrite	Chlorite	Plagioclase	Calcite	Dolomite	Gypsum	K Feldspar	Anatase	Illite/Smectite	Kaolinite	Siderite
	%	%	%	%	%	%	%	%	%	%	%	%	%
Mahantango, 7271'	47.2	34.5	3.1	9.7	5.6	0.0	0.0	0.0	TR	TR	0.0	0.0	0.0
Mahantango, 7391'	37.8	40.6	8.2	7.7	4.5	1.1	TR	TR	TR	TR	0.0	0.0	0.0
Marcellus, 7426'	44.4	32.3	10.0	6.6	4.0	2.8	0.0	TR	0.0	TR	0.0	0.0	0.0
Marcellus, 7430'	45.7	36.1	6.6	7.3	4.3	0.0	0.0	TR	0.0	TR	0.0	0.0	0.0
Marcellus, 7444'	45.1	37.3	5.3	5.5	4.8	0.8	1.1	TR	TR	TR	0.0	0.0	0.0
Marcellus, 7470'	42.9	38.8	5.1	3.5	6.2	1.5	2.0	TR	TR	TR	0.0	0.0	0.0
X-ray Mineral Services Ltd., North Wales													

Table 4. Mineralogical composition of Mahantango and Marcellus Shales determined by X-ray diffraction of whole rock samples.

Additional characterization done on the Mahantango and Marcellus Shales included measurements of grain density (by pycnometry), bulk density, and porosity. These results are summarized in Table 3, and will be used in analyses of water vapor diffusion rates

	Mahantango		Marcellus			
	7271'	7391'	7426'	7430'	7444'	7470'
grain density, g/cm3	2.78	2.79	2.79	2.80	2.72	2.63
bulk density, g/cm3	2.58	2.60	2.46	2.53	2.56	2.41
porosity	0.074	0.068	0.120	0.095	0.058	0.084

Table 5. Densities and porosities of Mahantango and Marcellus Shales used in vapor diffusion and adsorption studies.

Task 2.A. Shale water saturation versus water potential (water adsorption/desorption isotherms, and capillary pressure-saturation relations).

We obtain fairly complete water vapor adsorption-desorption isotherms on five different Woodford Shales during the first phase of this project, showing significant hysteresis over most of the measured water activity (relative humidity, rh, tested from 11% up to 96%). However, we identified two aspects of these equilibrium relations that remain to be understood. The first concerns quantifying the equilibrium relations at very high saturations associated with water-blocking of shales at fracture-matrix interfaces resulting from hydraulic fracturing fluid injections. The second concerns understanding vapor diffusion-limited rates for reaching equilibrium conditions farther away from the fully saturated regions. Both of these issues were addressed under the current project.

2.A.1. Extending adsorption-desorption isotherms to higher water contents and lower capillary pressures. Control of water potentials becomes prohibitively difficult above about 97% relative humidity, yet shale saturation relations are needed at these higher energies (lower capillary pressures) because they are expected to reflect conditions at fracture-matrix interfaces immediately following hydraulic fracturing. In order to fill this gap, we obtained measurements of water imbibition and drainage on the Woodford shale grains previously used for vapor adsorption-desorption measurements. These capillary pressure-saturation relations were obtained using a pressure plate system operated at 50 ˚C, over a capillary pressure range of 450 to 30 kPa (Figure 3). The pressure plate method is well suited for directly controlling P_c in this extremely high *rh* region, via controlling pressure differences above and below a porous ceramic plate [*Dane and Hopmans*, 2002]. We used a 500 kPa pressure plate in a 500 kPa chamber (Soilmoisture Equipment

Corp.), housed in an incubator maintained at 50 ± 0.5 ˚C. Compressed air was supplied to the chamber via a 2-stage pressure regulator, controlling P_c to within 1 kPa. A 1.0 M KCl solution was used to saturate the porous plate, and as the high ionic strength imbibing/draining solution for the shales. An open container of 1.0 M KCl was included in the pressure chamber in order to assure maintenance of *rh* ~1. The outflow tube from the pressure plate lead into the bottom of an outflow reservoir containing the same solution, and having its free surface of this reservoir kept at about 1 cm below the level of the pressure plate. This configuration allowed use of the pressure plate in both imbibition and drainage processes.

After shale samples reached vapor adsorption equilibrium at the highest applied *rh* = 0.96, they were transferred to 54 mm I.D. stainless steel sample rings for pressure plate equilibrations. Each sample ring was lined with a sheet of filter paper (Whatman 4), supported with linen gauze, and tightly secured to the ring with Kapton tape. When distributed onto the filter paper base of the sample rings, the thickness of the crushed shale pack was about 3 mm. The sample rings were placed onto the pressure plate, and the chamber pressure was raised to specific target P_c values. Moisture uptake and release from shale samples was monitored through periodically depressurizing the chamber and weighting sample rings as well as duplicate "blank" rings (taped, filter paper and gauze support). The three P_c values applied were 450, 100, and 30 kPa, and required equilibration times ranged from 6 to 21 days. No lower magnitude P_c levels were tested because they would have included progressively more significant contributions of pendular water between grain contacts. Upon reaching drainage equilibrium at 450 kPa, samples were returned to the *rh* = 0.96 chamber to initiate the series vapor desorption steps.

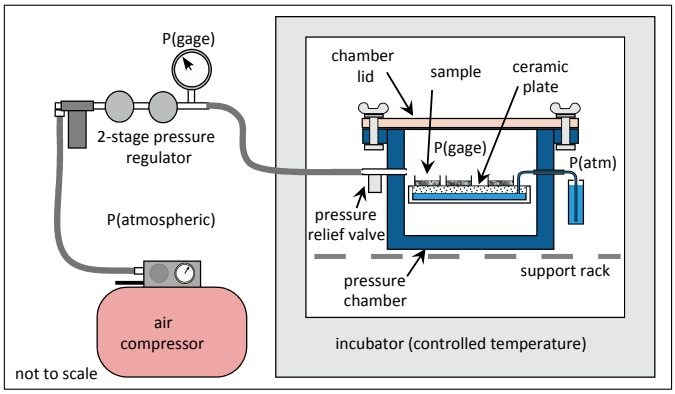

Figure 3. Pressure plate system for measuring imbibition and drainage on shale samples at moderately elevated temperature (50 ˚C).

Results of the composite results from water vapor adsorption/desorption isotherms (presented in earlier reports, and updated for the *rh* = 0.96 values) and imbibition/drainage capillary pressure measurements at 50 ˚C are shown in Figure 4. To the best of our knowledge, these are the first set of imbibition (adsorption) and drainage (desorption) measurements on shales that practically span the full range of moisture conditions, and that were obtained at elevated temperatures [*Tokunaga et al.*, 2017]. These composite results are presented in terms of variations in water:solid mass ratios with respect to *rh*. Water contents corresponding to full saturation (based on measured densities and porosities of grains, not of grain-packs) are indicated by arrows

along the y axes. Note that the curves from the 700 and 350 μm grain-size fractions of each shale sample were generally very similar, indicating that intragranular porosity and pore-size distributions were identical. These data clearly show hysteresis characteristic of equilibrium states of water in porous media, and show that substantial decreases in *rh* are required for removing water from the shale matrix. It is worth noting that these curves mostly show similar magnitudes of moisture retention at any given path-specific *rh*. The exceptions are associated with the WH1 samples that have substantially lower water contents. This was the only sample containing significant concentrations of inorganic carbon as calcite (3.61 mass % of C 11.7 mass % Ca, Table 1), consistent with less hydrophilic characteristics of carbonate surfaces [*Elgmati et al.*, 2011; *Morrow*, 1990; *Roychaudhuri et al.*, 2013]. Equivalent capillary pressures are provided along the upper x-axis of the WHf isotherms. Diameters of pores filling (or draining) as *rh* is varied, taken as twice the Kelvin radius are indicated along the upper x-axis for plots of the WR isotherms. The data collectively show that equivalent diameters of most of the pores are in the 1 to ~30 nm range. Note also that results from the pressure plate measurements are difficult to visualize here because they are associated with $rh > 0.99$.

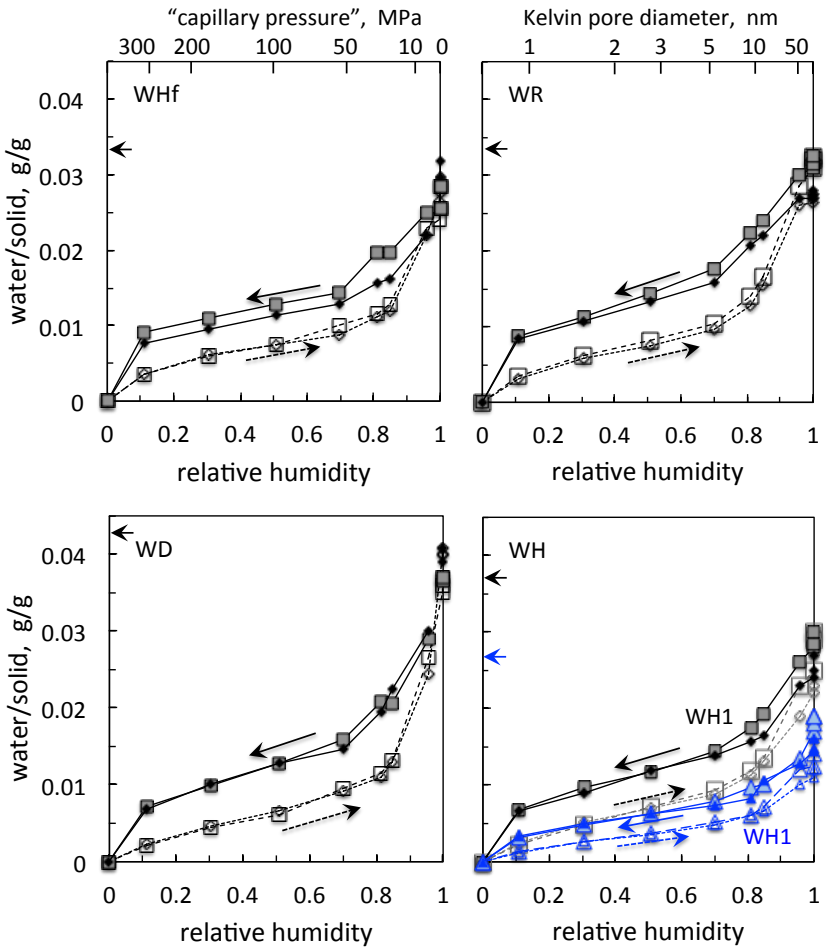

Figure 4. Adsorption and desorption isotherms for Woodford Shales at 50 ˚C. Refer to Table 1 for identifying characteristic of the individual samples. The 350 and 750 µm grain-size samples are indicated by smaller and larger data points, respectively. Adsorption and desorption paths are indicated with arrows along curves, respectively. Water:solid mass ratios corresponding to full saturation are indicated by arrows on the y axes.

The water adsorption/desorption and imbibition/drainage relations are plotted in terms of the water saturation dependence on the capillary pressure in Figure 5. For purposes of assessing water blocking, this representation of saturation relations is more immediately informative than the plots with respect to *rh* because magnitudes of P_c required to significantly desaturate shales are directly presented. The drainage (desorption) isotherms show that high P_c, generally in the range of ~1 MPa, are need in order to desaturate shales that have been expose to free water. Thus, regions within shale reservoirs that imbibe water-based hydraulic fracturing fluids require substantial water redistribution in order to allow return flow of gas. Given the very low matrix permeabilities of shales, the zones of elevated water saturation can be expected to propagate only short distances beyond fracture surfaces. However, low relative permeabilities substantially limit rates of water redistribution within matrix pores, thus allowing persistence of water blocks at fracture-matrix boundaries. These results underscore the challenge of moving either the gas phase or water phase through low permeability shales that have been exposed to water, sometimes referred to as the permeability jail phenomenon [*Shanley et al.*, 2004; *Shaoul et al.*, 2011]. A manuscript

summarizing this study on water potentials and capillary pressure controls on imbibition and drainage in Woodford Shales is near completion.

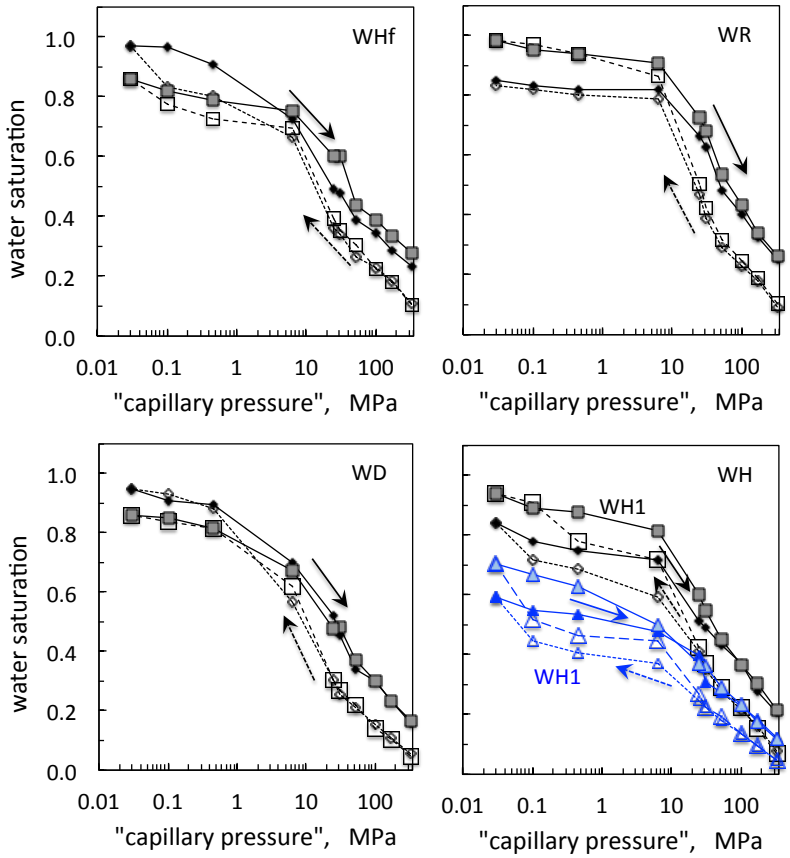

Figure 5. Adsorption and desorption isotherms for Woodford Shales at 50 ˚C, presented in terms of equivalent P_c. Refer to Table 1 for identifying characteristic of the individual samples. The 350 and 750 µm grain-size samples are indicated by smaller and larger data points, respectively. Adsorption (imbibition) and desorption (drainage) paths are indicated with arrows along curves, respectively.

2.A.2. Diffusion-controlled water vapor adsorption in Woodford Shales. All water vapor adsorption/desorption isotherms we reported previously were obtained on shales crushes to grain sizes less than 0.84 mm (passed through a #20 ASTM sieve). The 0.2 – 0.5 mm, and 0.5 – 0.84 mm size fractions of crushed shale from each of the five Woodford Shale wells was tested for water vapor adsorption-desorption at 50 ˚C. As noted in our earlier reports, the different size fractions yielded practically identical results, and reached equilibrium within one to several days. An example set of adsorption time trends is shown in Figure 6a. However, because the method requires periodic removal of samples from their controlled humidity chambers for weighing, high frequency measurements needed to determine rates of vapor transport into and out of grains would have imparted disturbances that would compromise quantification of diffusion. The relatively small grain sizes permit rapid equilibration, but short characteristic diffusion lengths (generally less than 400 µm into centers of even the largest grains) did not allow us to accurately track transient vapor diffusion.

In order to circumvent this limitation, we conducted experiments shale samples sliced into nominally 5 mm thick slabs, providing characteristic diffusion distances of about 2.5 mm. These new adsorption measurements are being obtained at 50 ˚C, 31% relative humidity, on a subset of Woodford Shales from the Roetzal (WR), Dunkin (WD), and Holt1 (WH1) cores. As shown in Figure 6b, adsorption equilibration times were on the order of 10s of days because of significantly longer diffusion length scale. Comparing Figures 6a and 6b, significant spatial variation in adsorption properties were encountered in the WD and WH1 shales, with the 5 mm sliced samples equilibrating at lower water contents than previously obtained on the crushed samples.

The diffusion-limited approach to adsorption equilibrium is evident from the approximately linear water uptake with respect to the square root of time during the early stages (Figure 6c). Modeling of water vapor adsorption time trends described in Task 4.A.1 yield effective diffusion coefficients useful for estimating rates of water redistribution within the shale matrix. However, the experimental approach did not allow distinction between diffusion along versus across shale bedding planes. In order to measure anisotropy in effective diffusion, a different approach was applied on samples of Mahantango and Marcellus Shales.

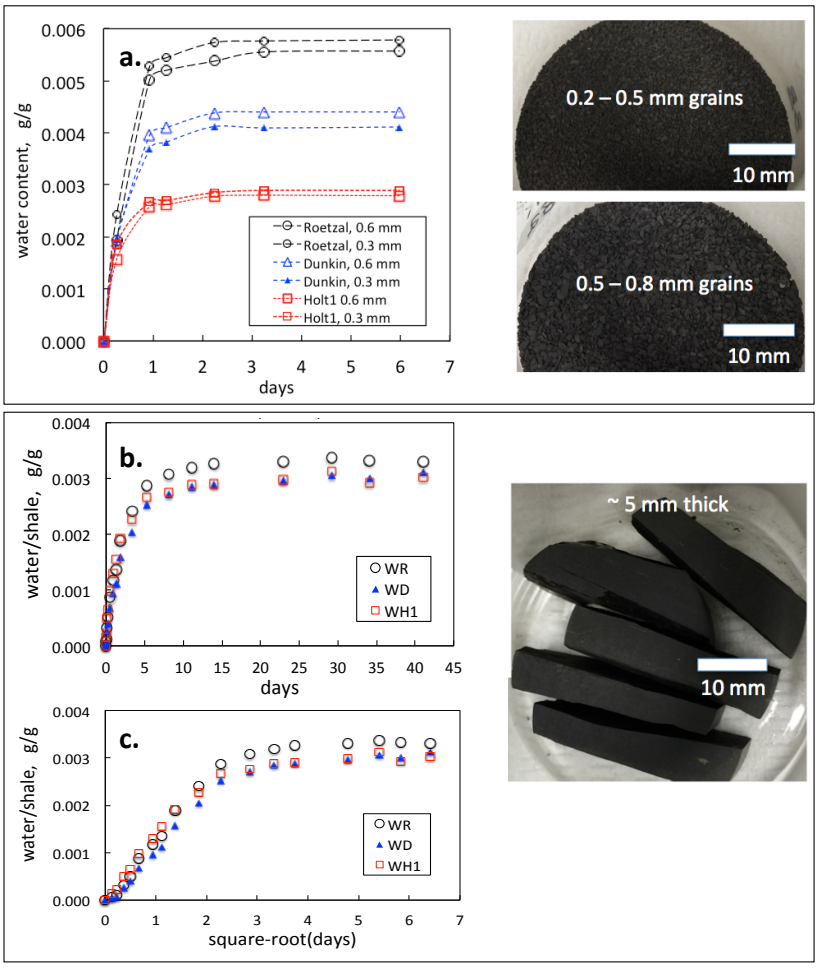

Figure 6. Comparisons of time-dependence of water vapor adsorption onto Woodford Shales continuously exposed to 31% relative humidity, 50 ˚C. **a.** Shale crushed to 0.2 to 0.5 mm and 0.5 to 0.8 mm grain size fractions. **b.** Shale sliced into ~ 5 mm thick laminae. **c.** Water vapor uptake versus square root of time for 5 mm thick shale laminae

Task 2.A.3. Testing anisotropy of water vapor diffusion in Mahantango/Marcellus Shales
Given the laminated structure of shales, effective diffusion coefficients and permeabilities within intact matrix blocks are expected to be strongly directionally-dependent (anisotropic), favoring transport parallel to the bedding plane. Such anisotropy is expected to facilitate gas flow horizontally towards vertical hydraulic fractures, while vertical flow across unfractured laminae is expected to be more restricted. Thus, measurements of the directional dependence of transport properties are needed to quantify the importance of anisotropy, and to provide input for larger scale modeling. Given the fairly generic nature of diffusive transport, these measurements are useful for quantifying anisotropy effects of not only water vapor but natural gas as well.

In order to quantify anisotropy in effective diffusion coefficients for vapor uptake, we are conducting experiments on shale samples that have either laminae edges or faces sealed. The overall experimental plan involves measuring water vapor diffusion at two different relative humidities (*rh*). The *rh* used in these diffusion experiments are 0.31 and 0.81, both at 50 ˚C, in order to determine impacts of different levels of pore filling by capillary condensation. Acknowledging the limitations of estimating pore radii (*r*) with the Kelvin equation [*Seemann et al.*, 2017], the *rh* = 0.31 and 0.81 correspond to filling of pores with *r* up to very approximately 0.8 and 4 nm, respectively. The sequence of sample preparation and testing is illustrated in Figure 7, and briefly listed here. **1.** seal cylindrical (lateral) walls of cores with epoxy and Al foil to allow vapor entry only exposed edges of bedding planes (diffusion parallel to bedding planes); **2.** oven-dry the laterally sealed samples; **3.** place cores into a *rh* = 0.31 chamber and monitor water vapor uptake until equilibrium is reached; **4.** transfer samples into a *rh* = 0.81 and continue monitoring water vapor uptake until the new equilibrium is reached; **5.** remove lateral seals (epoxy and Al foil), further cut and reseal these core plugs to allow diffusive entry only in the direction normal to the bedding plane; **6.** oven-dry samples; **7.** measure transient vapor uptake at *rh* = 0.31 until equilibrium is reached; and **8.** measure vapor uptake at *rh* = 0.81. Prior to initiation of each vapor diffusion-adsorption run, oven-dried samples were pre-equilibrated at 50 ˚C in a vacuum desiccator. Because of unanticipated long equilibration times encountered in step 7, we were not able to initiate the final run at *rh* = 0.81. It should be noted that open surfaces of the shale samples were sanded (P800, then P1200 grit corundum) to assure removal of excess epoxy. Photographs of the sidewall core sections used to measure vapor transport parallel to and perpendicular to bedding planes are shown in Figure 8. The *rh* = 0.31 and 0.81 conditions were controlled with reservoirs of saturated aqueous $MgCl_2$ and KCl solutions, respectively [*Greenspan*, 1977], contained in an incubator kept at 50 ±0.5 ˚C.

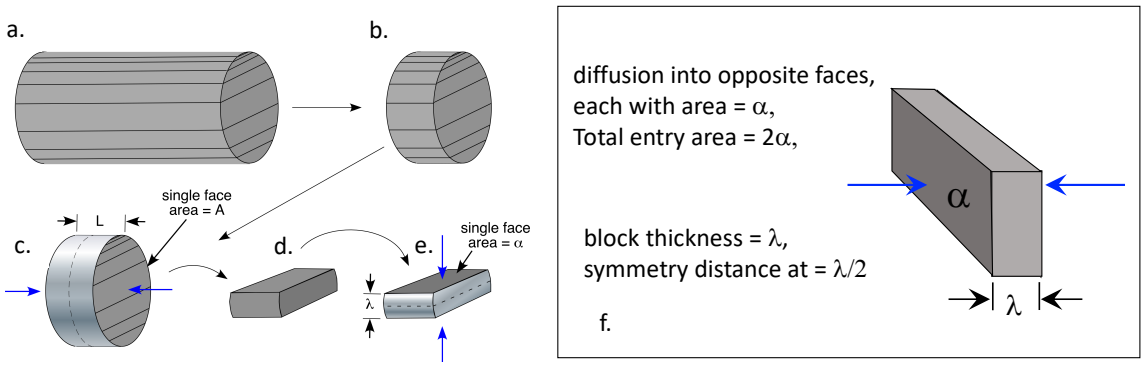

Figure 7. Sequence of preparing sidewall core plugs for measurements of water vapor diffusion/adsorption along and across bedding planes. **a.** sidewall core plug showing bedding planes alone original core axis. **b.** sliced core disc. **c.** core disc sides sealed to allow vapor diffusion only along bedding planes, entering from unsealed opposite faces. **d.** core disc cut to obtain slab sample. **e.** edge faces of slab sample sealed to allow vapor diffusion only by diffusing across bedding planes. **f.** geometry for vapor diffusion across bedding planes from opposite faces.

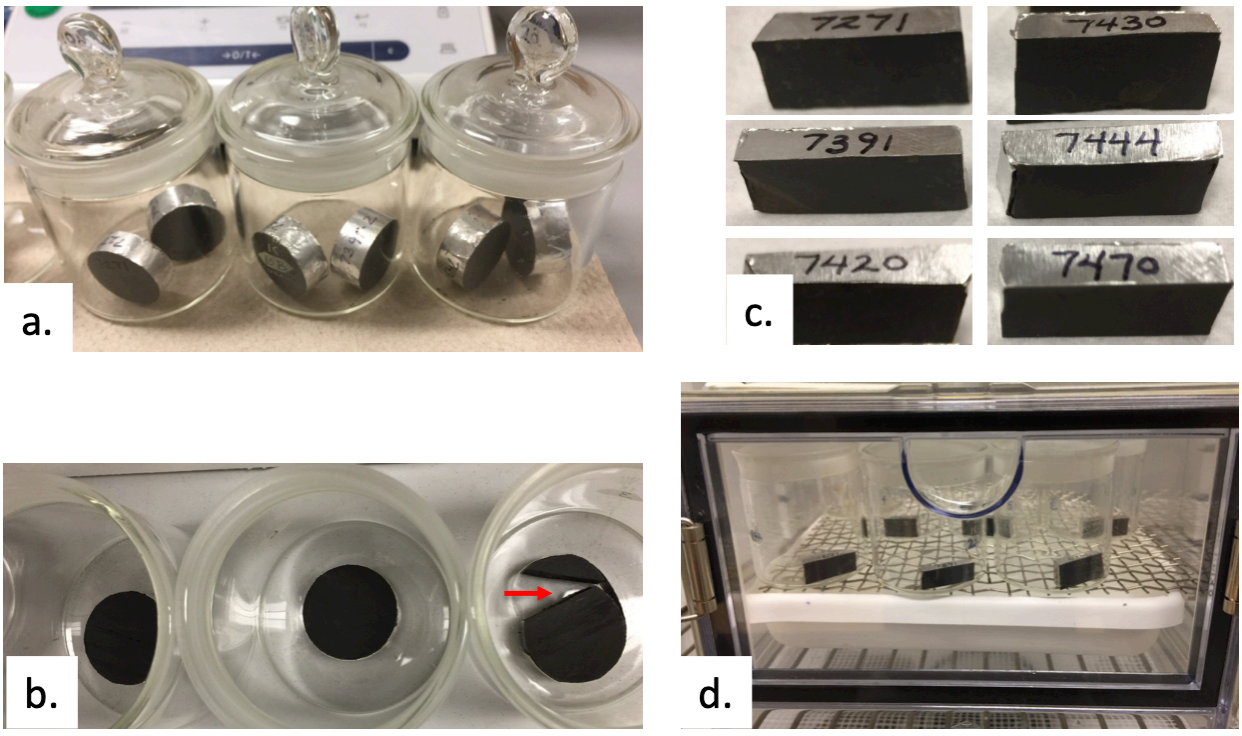

Figure 8. Photographs of Mahantango and Marcellus Shale samples used in water vapor diffusion/adsorption experiments. **a.** Several of the parallel to laminae diffusion samples in weighing jars. **b.** Several samples at the end of run at *rh* = 0.81. Note the expanded-split sample 7426 (red arrow). **c.** Perpendicular to laminae diffusion samples. **d.** Perpendicular to laminae diffusion samples in *rh* = 0.31 (50 ˚C) enclosure.

Water vapor uptake in the shales was initially rapid in all samples, followed by declining rates typical of diffusion limited processes. The blank control sample showed no significant mass change throughout the experiment, demonstrating that hydration of the epoxy and foil contributed negligibly to water uptake. The time dependence of water mass uptake per unit mass of shale at *rh* = 0.31 presented in Figures 9a and 9c shows that Mahantango samples 7271 and 7391 behave very similarly, and equilibrated at lower water contents relative to the Marcellus samples. The initial 3 days of water vapor uptake proceed approximately in proportion to the square-root of time (Figure 9b and 9d), indicative of the time scale over which the diffusion front has not extended to the L/2 distance.

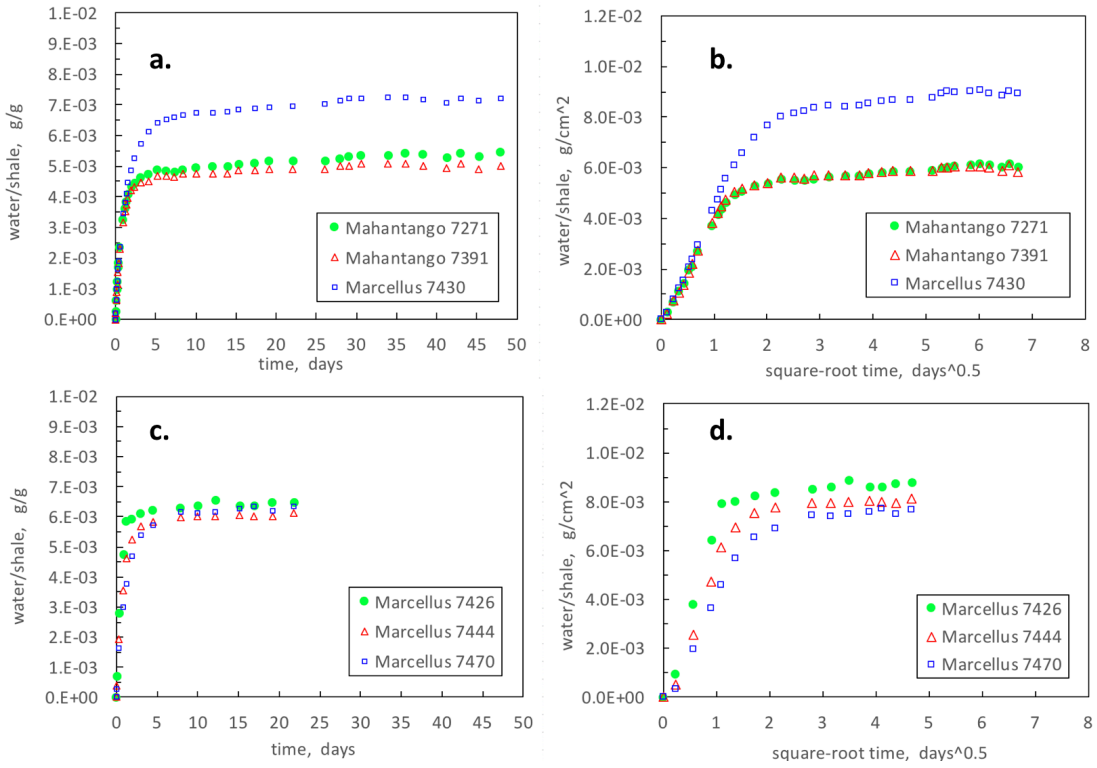

Figure 9. Water vapor diffusion and adsorption in Mahantango and Marcellus Shale cores, with entry occurring parallel to the bedding plane. Exposure of dry cores to *rh* = 0.31 at 50 ˚C. **a and c.** Time-dependence of water mass uptake per unit shale mass. **b and d.** Water mass uptake per unit entry surface area, versus square-root of time.

After reaching water vapor adsorption equilibria at *rh* = 0.31, the core samples were transferred into the *rh* = 0.81 chamber and periodically weighed to monitor water uptake at this higher humidity. Water vapor uptake rates at *rh* = 0.81 with respect to time and square-root of time are shown in **Figures 10 a,c** and **10 b,d**, respectively. Notable differences relative to behavior at the lower *rh*, are the much greater levels of water uptake, and require much longer times to approach equilibrium. The latter behavior is consistent with both impeded diffusion as capillary condensation becomes increasingly important in blocking vapor transport and slow pyrite oxidation. Indeed, even after 128 days of uptake, equilibrium was not achieved. In the interest of moving to the measurements of vapor diffusion tranverse to the laminae, this set of uptake measurements was ended, and samples were oven-dried. Even after 2 days of drying at 110 ˚C,

followed by cooling to room temperature in a vacuum desiccator, some samples showed significant increases in mass. In particular the Marcellus 7426' sample containing an initial pyrite content of 10% exhibited a mass increase of 0.021 g g^{-1} relative to its initial dry state. Arrows along water content axes of Figures 10a and 10b indicate the relative mass increase.

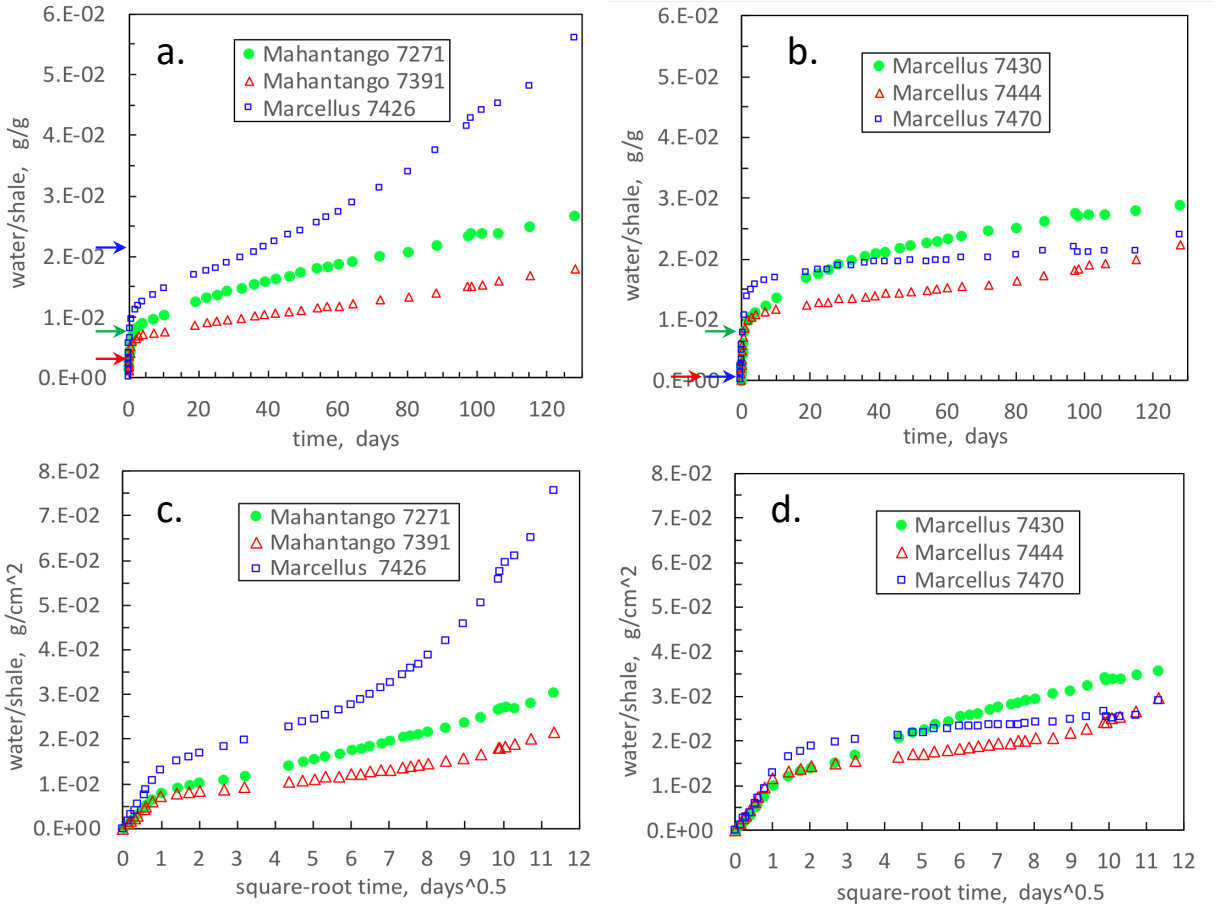

Figure 10. Water vapor diffusion and adsorption in Mahantango and Marcellus Shale cores exposed to *rh* = 0.81 (50 ˚C), with entry occurring parallel to the bedding planes. Cores were previously equilibrated at *rh* = 0.31 (50 ˚C), and uptake is relative to water contents achieved at the end of the previous equilibration (*rh* = 0.31). **a and b.** Time-dependence of water mass uptake per unit shale mass. **c and d.** Water mass uptake per unit entry surface area, versus square-root of time. Arrows along water content axes of Figures 10a and 10b indicate dry mass increase after 2 days of drying at 110 ˚C, followed by cooling to room temperature in a vacuum desiccator.

After drying, the cores used in the experiments at *rh* = 0.81 were cut to obtain smaller samples that were sealed along "edge" surfaces to allow measurement of vapor diffusion across shale laminae (Figure 7d-f). The slab samples were dried, placed in individual weighing jars and incubated at *rh* = 0.31 (50 ˚C), periodically briefly removed for weighing to monitor water uptake. Trends in measured water mass uptake per mass of dry shale are plotted with respect to time and square-root of time in Figures 11a and 11b, respectively. Note that the diffusive uptake of water vapor remained linear with respect to the square-root of time for about 11 days, before beginning to asymptotically approach equilibrium. It should also be noted that equilibrium has still not been

reached in some of the samples (latest data from day 133), despite the fact that the diffusion distances to sample midplanes (λ/2 in Figure 1f) were only 2.2 to 2.9 mm. In contrast, the earlier measurements at *rh* = 0.31 for diffusion-controlled uptake along the bedding planes remained linear with respect to square-root of time over only the initial ~4 days, and appeared to reach equilibrium adsorption within about 30 days, despite longer diffusion distances (L/2 in Figure 1c) of 4.5 to 5.5 mm. Although slow pyrite oxidation is likely contributing to continued mass increases, comparisons of short-term uptake rates parallel versus transverse to bedding planes is still useful for estimating the extent of anisotropy in effective diffusion coefficients. A rough estimate of anisotropy for effective diffusion coefficients parallel versus transverse to bedding is 5.7:1, obtained from the short-term ratios of diffusion lengths per square-root of time.

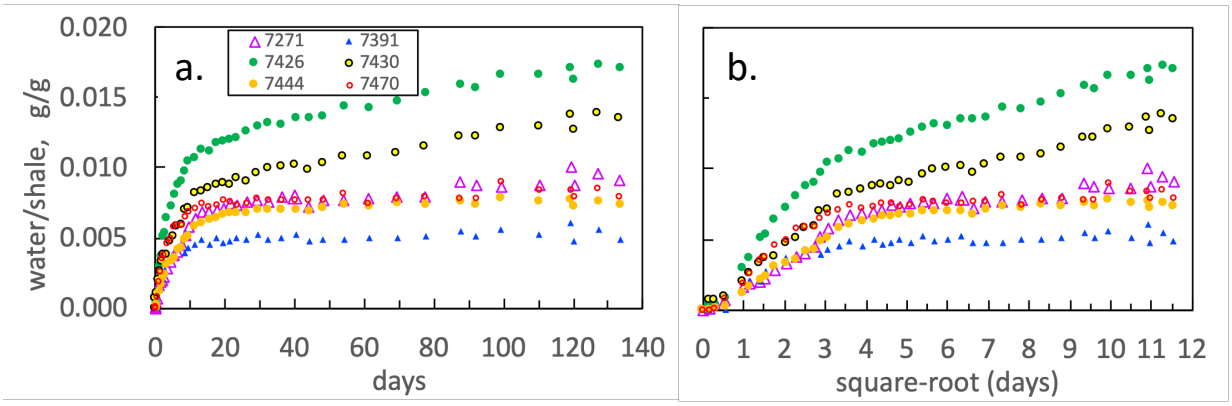

Figure 11. Water vapor diffusion and adsorption in Mahantango and Marcellus Shale cores, with entry occurring across the bedding planes. **a.** Time-dependence of water mass uptake per unit shale mass. **b.** Water mass uptake per unit shale mass, versus square-root of time.

Task 2.B. Water Imbibition into shale.

These tests were originally intended to be conducted on sidewall core plugs at elevated pressures and temperatures, under confining pressures in excess of 10 MPa. However, the few available intact Mahantango and Marcellus core plugs were relatively short, and several were damaged during the process of loading and prestressing in the core holder (Figure 12). Therefore, imbibition tests were only run at room temperature and atmospheric pressure. Shown are results for imbibition from a water source maintained at -40 mm capillary pressure, entering into the sidewall core from the 7221' and 7326' depths. Similar atmospheric pressure water imbibition measurements were obtained on Woodford Shales in the previous phase of this project, and modeling of those experiments is presented in Task 4.B. In Figure 13, note that the water uptake versus square-root of time plots are relatively linear, indicating that the shales behave macroscopically as an approximately hydraulically homogeneous porous medium. It should be noted that these core samples contained hydraulically continuous microfractures evident from initially steeper slopes in the square-root time plots. It is also worth noting that even after 2 days of imbibition, the wetting front entered only a few mm, underscoring the shallow extent of water blocked region in low permeability shales. The interdependence of these imbibition rates on permeability, porosity, wettability, and fluid viscosities are currently being compared with several approaches proposed for capillary scaling [*Busch and Amann-Hildenbrand*, 2013; *Mason and Morrow*, 2013; *Schmid and Geiger*, 2013].

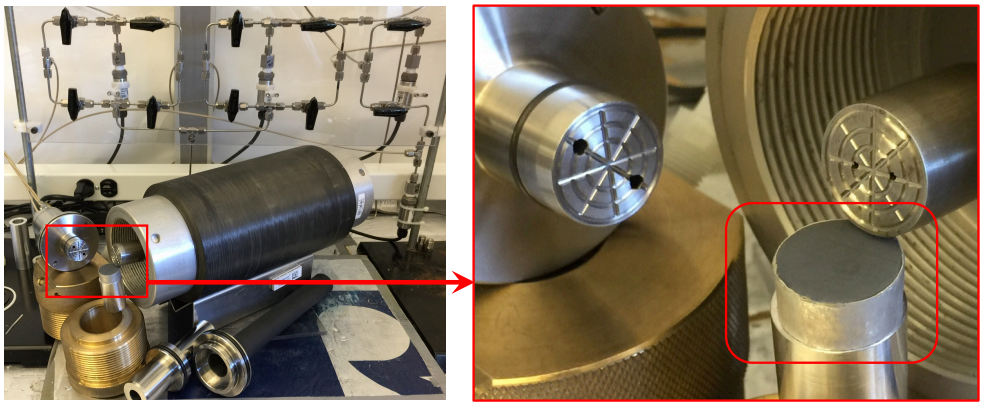

Figure 12. High pressure core system, modified to accommodate small sidewall cores.

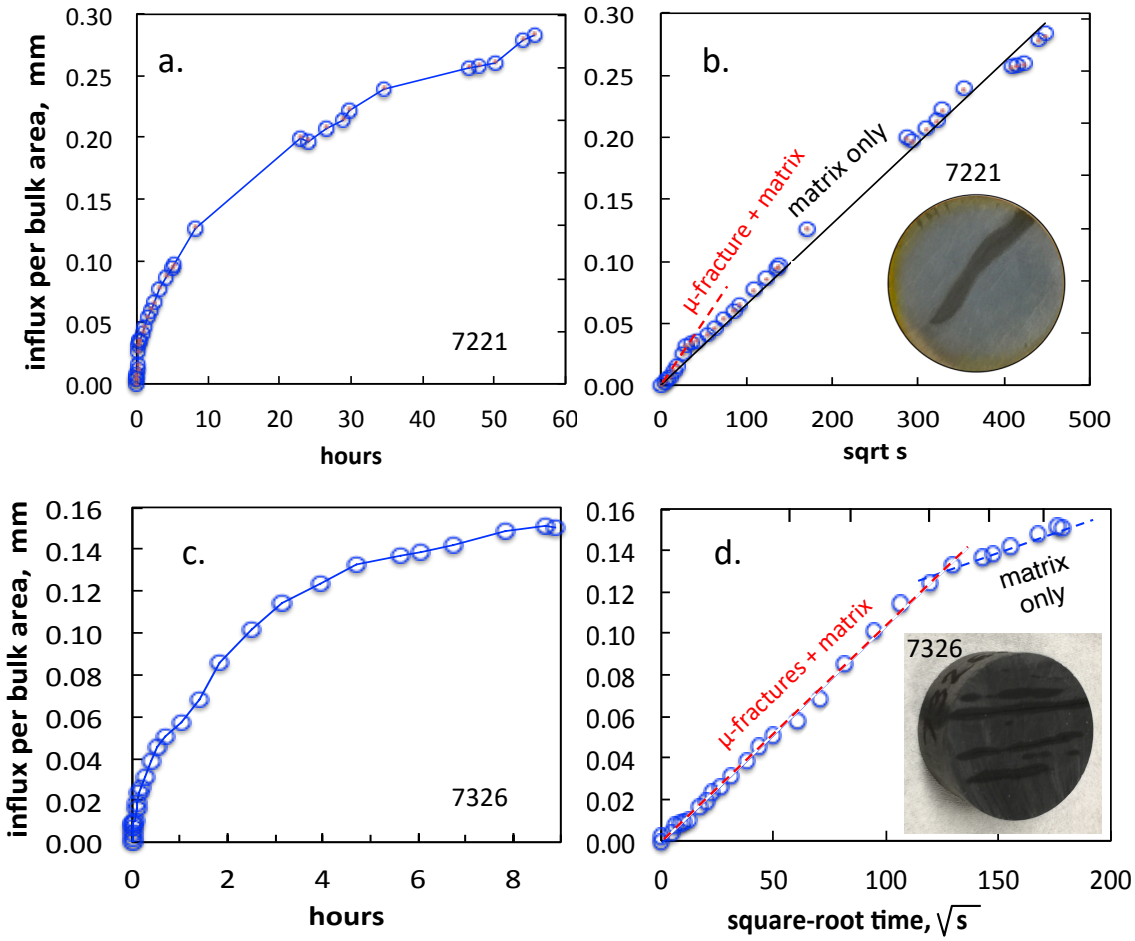

Figure 13. Water imbibition into the sidewall shale sample from 7221' and 7326' depths. The water source capillary pressure is maintained at -40 mm, and water uptake is plotted with respect to (**a., c.**) time and (**b., d.**) square-root of time. Note that enhanced water uptake in the cores' microfractures are evident from the higher initial slopes in square root time plots (dashed red lines, panels **b**., **d**.).

Task 2.C. Methane adsorption in partially saturated shales

The experimental component of a study on the influence of partial water saturation in shales on methane adsorption was completed by Lu Wang in our laboratory during the beginning of this project. That work utilized crushed shale samples from the Qaidam Basin, China, equilibrated with water at fixed *rh* ranging from 0.22 up to 0.89 (40 ˚C) prior to methane exposure. Methane adsorption isotherms were measured at pressures up to about 9.3 MPa, and was later modeled in order to examine impacts of water blocking and competitive adsorption of water versus methane on shale surfaces. Results showed that methane adsorption is reduced by up to 45% as water activity is increased, but that the impacts of water become insignificant at $rh \geq 0.75$. Water vapor adsorption isotherms and methane adsorption isotherms obtained at different water contents on one shale sample are shown in Figure 14. This work has just recently been published [*Wang et al.*, 2018].

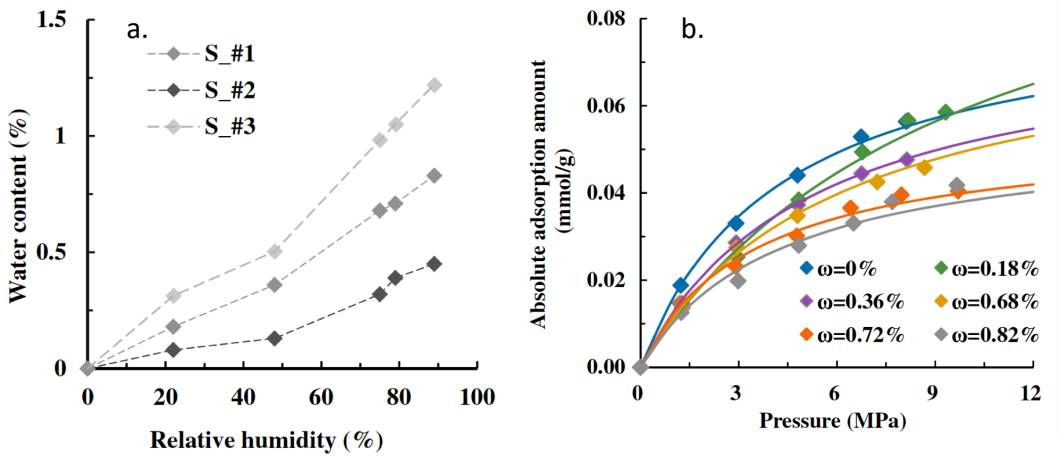

Figure 14. Water content influences on methane adsorption. **a.** Water vapor adsorption isotherms on three shale samples. **b.** Methane adsorption isotherms obtained at different water contents in shale #1.

Task 3. Non-water fracking fluids experiments for reservoir stimulation

This task was added to the existing project in 2017. The ultimate goal of this task was to better understand the influence of fracturing fluids, specifically water-based vs. CO_2-based, on shale oil mobilization. The scope, limited by funding constraints, had two subtasks. One was to design and construct a high pressure and temperature fracture-matrix microfluidic device with different wettability, which allows pore-network scale visualization experiments on transient water/CO_2 (fracturing fluid)-oil counter flow. Another subtask was to design and construct a high pressure/temperature foam generator for testing efficiency of foams for displacing hydrocarbons from deep reservoirs. This new system differs from the conventionally used approach of co-injecting fluid phases through a sand-packed column in order to generate foams. Thus, viscosities of CO_2-based fracturing fluids can be tested over longer times relative to single-pass systems. In the past two years we have made significant progress on both the high pressure micromodel system and foam generation, including publication of our first paper on generation of $scCO_2$-foams [*Wan et al.*, 2017]. These newly designed laboratory capabilities are ready to be used for future applied scientific discoveries.

Task 3.A. Design and construction of fracture-matrix micromodels with different wettability

We designed and constructed a set of fracture-matrix micromodels with both homogeneous and heterogeneous pore and fracture geometries. We tested different methods to alter the wettability of the micromodels. Now we can controllably alter the wettability to water-wet, intermediate-wet and oil-wet. The multiphase fluid control system is designed for use with oil, water, and foams including $scCO_2$-based foam in manipulating the viscosity and chemistry (control interfacial properties) (Figure 15). This system is ready to be used in understanding mechanisms of EOR at pore scale, and helping the developing new methods to increase oil production.

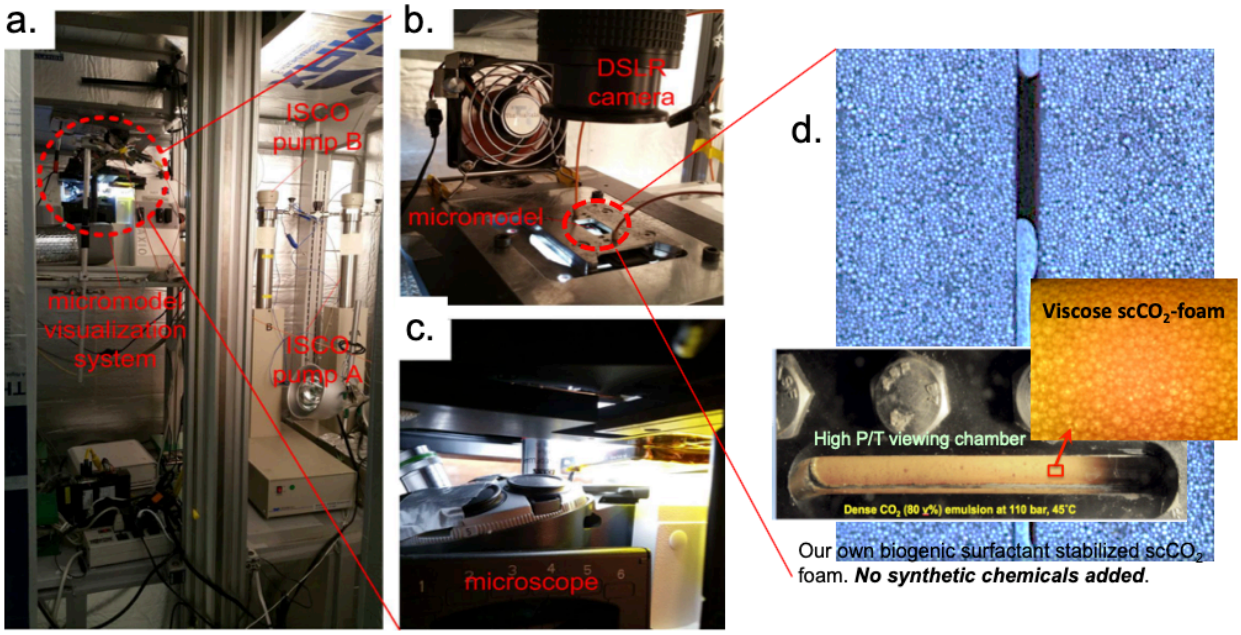

Figure 15. Our newly modified high pressure and temperature microfluidics setup, and fracture-micromodel for multi fluids displacement studies (Wan et al., Energy & Fuels, 2017).

Task 3.B. Design and construction a high pressure/temperature foam generator

The sand-packed column approach has been conventionally used in laboratory foam generation. The shortcoming of this approach is its inefficiency, because the column is easily clogged by surfactant and chemical aggregates which needs to be frequently repacked in each usage. Furthermore, the approach is limited to single-pass generation and foam testing. We decided to design a blender-based foam generator based on a system introduced by Hutchins and Miller [*Hutchins and Miller*, 2005], suited for fluid recirculation, and quick testing many different combinations of surfactants and ratios of fluids, different shear stresses, controlled pressures and temperatures.

Over the past two years, several variations of the foam generator were tested and modified. The latest design shown in Figure 16 includes the high-speed blender (micropump) for making the foam, rheometer system for viscosity measurement and viewing window for foam imaging. The operation pressure ranges up to 80 MPa, accommodates wide ranges of fluid ratios containing desired surfactants and nanoparticles, and runs at temperatures up to 200 ˚C (all parts sets inside

an oven incubator). Example tests shown in Figure 17 were obtained with recipes based on Xue et al., 3.6% SLES (STEOL CS 330) in 2% NaCl (instead of KCl) [*Xue et al.*, 2016]. The figure shows a plot of viscosity as a function of quality (percentage of CO_2). The viscosity reached 17 to 22 cP at 70% to 85% foam quality (% volume of CO_2). It should be noted that Xue et al. (2016) reported much higher viscosities using the sand-packed column method for foam generation, and that their viscosity starts to climb between 90 and 95% foam quality. This large discrepancy needs to be understood in the future study.

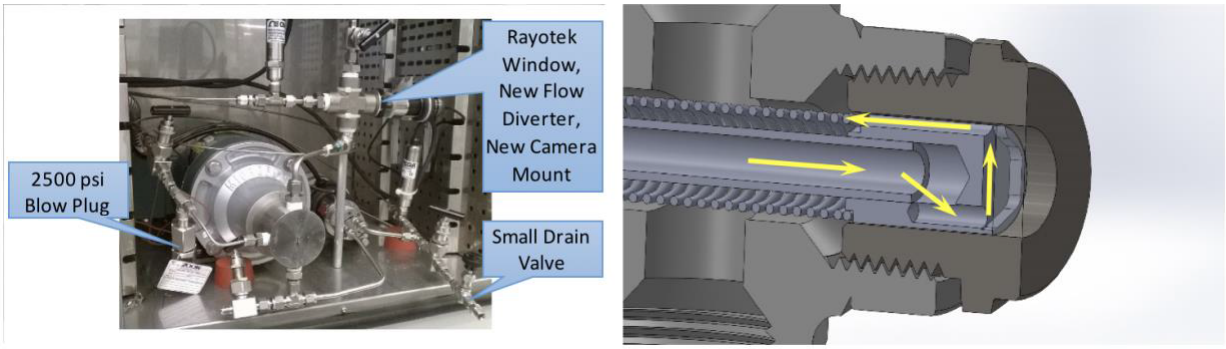

Figure 16. Foam generator/rheometer system and viewing window.

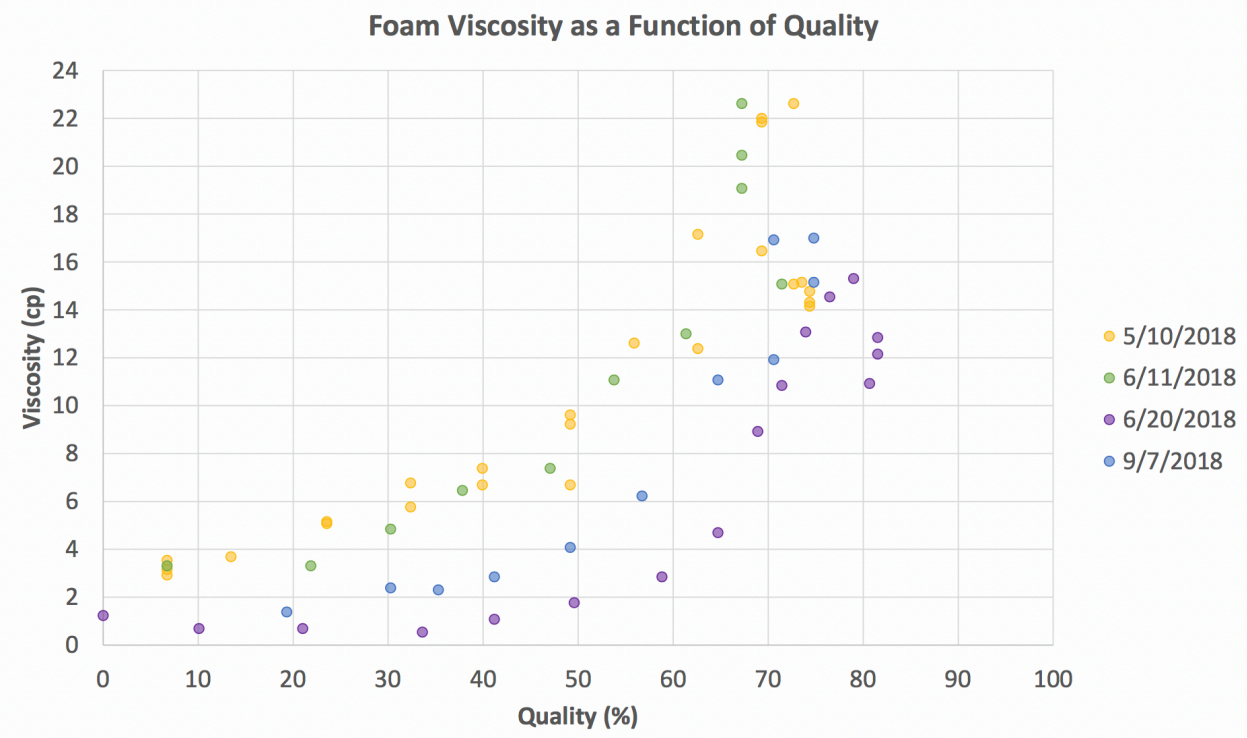

Figure 17. Measured effective viscosities versus foam quality (volumetric % CO_2) at 9 MPa, 25 ˚C. Tergitol solutions (5-10-18 and 6-11-18), and STEOL solutions (6-20-18 and 9-7-18).

Task 4. Modeling studies for understanding fluid flow and transport processes in shale matrix and matrix-fracture interfaces

Task 4.A. Improve and apply multiphase flow models for shale

The main objective in this task was to improve the knowledge on the macroscopic nature of water and non-water flow and entrapment in shale matrix and across matrix-fracture interfaces, and ultimately to develop upscaling strategies and continuum modeling approaches. During this phase of the project, we mainly focused on understanding diffusion, adsorption and capillary condensation in shale by using the experimental data generated in Task 2. A summary of our research findings from this task is summarized in two parts below. In the first part, we applied a water vapor diffusion and adsorption model to characterize the magnitudes of anisotropic effective diffusion coefficients in shale samples under low relative humidity conditions (RH=0.31). In the second part, we developed a new continuum multiphase multicomponent model and applied to the experiments conducted under high relative humidity conditions (RH=0.81), involving coupled processes of diffusion, adsorption and capillary condensation.

Task 4.A.1 Estimating Anisotropic Binary Diffusion Coefficients in Shale Using Experimental Data

In this part of the task, we assessed the major diffusive transport processes with sorption in Woodford shale laminae samples and Marcellus shale core plugs. Our modeling and experimental results for the Woodford shale laminae samples were presented in the earlier progress reports and a paper [*Tokunaga et al.*, 2017].

We employed both numerical and analytical modeling approaches to estimate the magnitudes of the effective diffusion coefficients in the shale samples. The numerical model is based on solution of the Maxwell-Stefan diffusion equations for a binary mixture of water and air, including Knudsen diffusion and adsorption. Surface diffusion of water along pore walls may also be important [*Krishna and Wesselingh*, 1997], but its affect was assumed to be lumped into the Knudsen diffusion coefficient. In the continuum limit, where the mean free path of gas phase molecular collisions (l_o) is small relative to the characteristic pore radius (r_o), the diffusion coefficient for water vapor through air is taken as the product of a gas porosity-dependent tortuosity factor $f(\varepsilon)$ times the binary molecular diffusion coefficient in the bulk gas phase denoted by D_0. The Knudsen contribution accounts for the influence of vapor phase water molecule collisions with pore walls [*Loeb*, 1961; *Wesselingh and Krishna*, 2000], with its diffusion coefficient is denoted by D_K. In the analytical model, Maxwell-Stefan diffusion effects considering interaction between different molecule types are ignored, and Fickian diffusion is assumed. In that case, the effective diffusion coefficient can be given as $D_{eff} = 1/[1/D_K + 1/(f(\phi)D_0)]$ or equivalently $D_{eff} = f(\phi)D_0/(1+Kn)$, which are forms of Bosanquet's equation for gas diffusion in porous media, accounting for Knudsen effects [*Pollard and Present*, 1948; *Tokunaga*, 1985]. $Kn = l_0/r_0$ denotes the Knudsen number, i.e., the ratio of the gas mean free path to the characteristic pore radius (r_o). For H_2O diffusing through a gas phase consisting primarily of N_2 (78%) and O_2 (21%), an estimated collision diameter σ = 0.31 nm was obtained from averaging of kinetic diameters [*Li et al.*, 2009; *Loeb*, 1961; *Massman*, 1998]. The mean free path for H_2O vapor diffusion in air was then estimated from kinetic theory [*Loeb*, 1961] as $l_0 = k_B T/(\sqrt{2}\pi\sigma^2 P)$, which at 50 ˚C and local atmospheric pressure (98 kPa) gives l_o = 110 nm.

Based on our model comparisons using the same input parameters, the differences between the more general numerical model and the analytical model are negligible. Therefore, we employed the analytical solution to fit the experimental data for characterizing diffusion coefficient and adsorption parameters. For the small value of the relative humidity in the measurements used, a linear adsorption model can be used to represent the adsorption of water molecules on solid phases in shale matrix (C_s [kg/kg]=K_d[m^3/kg]×C_{H2O}[kg/ m^3]). For the analytical model, we modified an existing solution [*Ozisik*, 1980] in the heat transfer context and then developed a computer code to evaluate the analytical solution for the diffusion and the linear adsorption in a rectangular parallelapiped domain to represent the experimental data in Woodford shale block samples. Table 6 summarizes the results for the diffusion coefficients and sorption coefficients (K_d) for Woodford shale blocks. Effective diffusion coefficients in the range of 9×10^{-9} to 3×10^{-8} m^2/s are consistent with other measurements on low-porosity rocks [*Peng et al.*, 2012; *Tokunaga et al.*, 2017].

We conducted similar analyses for assessing the diffusive transport processes with adsorption in Marcellus shale core plugs. To fit the experimental data, we employed a one-dimensional analytical solution for diffusion and sorption in a finite domain with fixed vapor concentrations at both ends, as in our experimental conditions (Task 2), parallel to laminae. We modified the analytical solution given in Crank for similar initial and boundary conditions [*Crank*, 1975]. Table 7 summarizes the results for the Marcellus shale samples. We presented below summary of the results based on the interpretations of the data using our modeling studies. As in the Woodford samples, the diffusion occurs mainly under Knudsen regime. The effective diffusion coefficients of the Marcellus samples appear to be an order of magnitude greater than the effective diffusion coefficients of the Woodford samples, while the sorption coefficients of the Marcellus samples are 2 to 4 times smaller. This might be due to presence of larger pore connectivity and larger pore sizes in the Marcellus rock samples.

Comparisons between measured water vapor uptake in the Woodford shale samples and model results with the best fit parameters are shown in Figure 18a. Our estimations indicated that the Knudsen diffusion would be the dominant diffusive transport process for water vapor diffusion into shale under our experimental conditions, with individual water molecules colliding primarily with shale pore surfaces. The nature of the diffusion process becomes also evident upon combining the value of l_o = 110 nm determined earlier for water vapor diffusion in bulk air at 50 ˚C and 28 kPa. With most of the pore space associated with pore radii ranging from 2 to 5 nm based on the estimations from the adsorption-desorption data, $Kn = l_o/r_o$ ranges from about 50 to 20. Table 8 presents the estimated effective water vapor diffusion and adsorption coefficients in the direction perpendicular to lamination. The effective diffusion coefficient in the perpendicular direction is estimated to be one order of magnitude less than the diffusion coefficient values in the parallel direction.

Table 6. Estimated model parameters for Woodford shale laminae samples.

	WR	**WD**	**WH1**
Porosity	0.081	0.106	0.063
Estimated D_{eff}, m^2 s^{-1}	**1.48×10^{-8}**	**9.06×10^{-9}**	**2.78×10^{-8}**
Estimated K_d, m^3 kg^{-1}	0.126	0.115	0.112

Table 7. Estimated model parameters for Marcellus shale samples (parallel to lamination).

	7271	7391	7430
Porosity	0.068	0.076	0.091
Estimated D_{eff}, $m^2\ s^{-1}$	**6.08×10^{-7}**	**6.05×10^{-7}**	**4.38×10^{-7}**
Estimated K_d, $m^3\ kg^{-1}$	0.205	0.195	0.279

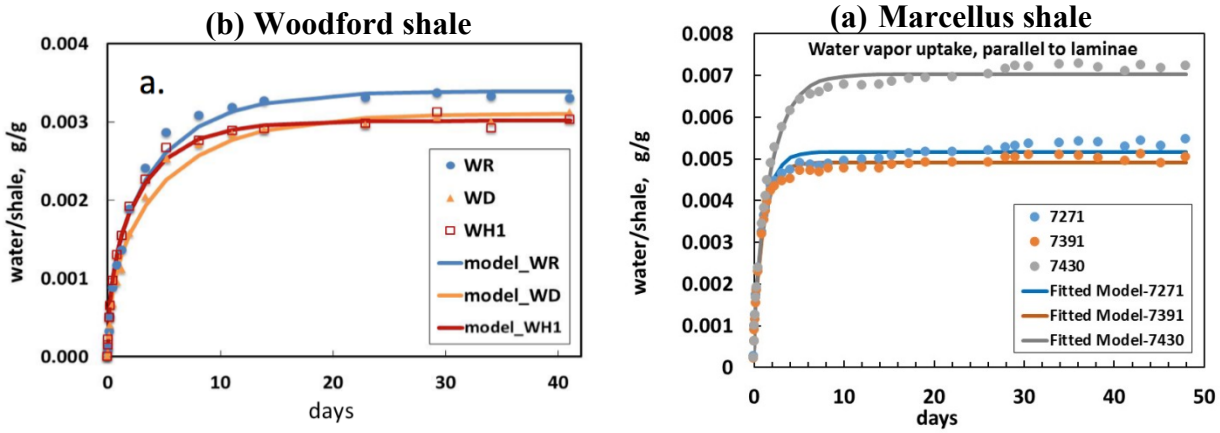

Figure 18. Comparisons between measured and modeled time-dependence of water vapor adsorption onto (**a**) Woodford Shales, and (**b**) Marcellus shales (also see Figure 9a).

Table 8. Estimated model parameters for Marcellus shale samples (perpendicular to lamination).

	7271	7391	7430
Porosity	0.074	0.067	0.095
Estimated D_{eff}, $m^2\ s^{-1}$	**3.60×10^{-8}**	**4.18×10^{-8}**	**2.75×10^{-8}**
Estimated K_d, $m^3\ kg^{-1}$	0.315	0.192	0.408

Task 4.A.2 Assessing Multiphase Flow and Transport Processes in Shale Using a New Model: Multicomponent diffusion, adsorption and capillary condensation in Shale Matrix

A further investigation of the nature of the transport processes, formation of capillary condensed liquid water higher relative humidity conditions was conducted in the second part of this research task. Under high relative humidity conditions (0.81), condensation of water vapor and formation of liquid phase in shale pores need to be taken into account. Strong molecular interactions between fluid molecules and solid molecules exist in nanoscale pores of shale matrix. The fluid-solid interaction forces in shale pores can significantly influence the distribution of the multiphase fluids. Understanding the interaction forces on fluids in shale pores and incorporating those fundamental processes into continuum models are needed to investigate and find practical approaches to improve oil and gas recovery. This motivated us to develop and apply a new modeling approach to explicitly represent the fluid-solid interaction forces in shale, because the traditional two-phase modeling approach is known to have limitations in representing those processes in shale.

In this task, we developed an initial version of a new multiphase multicomponent model based on the density functional approach [*Armstrong et al.*, 2016; *Dinariev and Evseev*, 2017; *Rowlinson and Widom*, 1982; *van der Waals*, 1894], which led to development of new set of continuum balance equations. The equations explicitly include interaction forces between fluids and solids that influence multiphase processes at continuum scales of shale. This new model will be referred as DFM, density functional model. A brief explanation of DFM is presented below, which is followed by an application to explore the sustained disequilibrium phenomenon and multiphase behavior with vapor diffusion and capillary condensation in shale rock samples in the Marcellus shale experiments in Task 2.

Theoretical Basis of the DFM Approach

Our starting point in the derivation is to define the free energy of the multiphase mixture as the density functional depending on molar concentrations. The theoretical developments below are given for isothermal conditions, but similar theoretical development leads to models under non-isothermal conditions. Description of the free energy density function as a function of molar densities has a long history. It goes back to *van der Waals* theory (1893) that is known to be the first to use the energy density functional for describing the interfaces between two fluid phases with a single component. Later, Cahn and Hillard extended the theory for binary mixtures in a two-phase system [*Cahn and Hilliard*, 1958]. The similar concept was successfully used in quantum mechanics to represent the energy of molecules as functions of electron density and named density functional theory [*Hohenberg and Kohn*, 1964; *Kohn*, 1999]. For hydrodynamic applications, Dinariev presented a generalization of the density function approach for multicomponent multiphase fluid systems and named density functional hydrodynamics [*Dinariyev*, 1995]. Recent applications at the pore-scale include representation of pore-scale multiphase flow phenomena, including imbibition, drainage, capillary condensation and adsorption at pore walls [*Armstrong et al.*, 2016; *Dinariev and Evseev*, 2017].

Here, we extended the application of the density functional approach to derive continuity and momentum balance equations for multiphase mixtures and to obtain a new mathematical model for continuum representation of multiphase multicomponent flow in porous media. The Helmholtz free energy of an inhomogeneous system at a constant temperature can be expressed as

$$E_H = \int_V \psi \, dV \tag{1}$$

where ψ is the local energy density defined as the free energy per unit volume of a rigid porous medium. Considering the gravitational potential and the interaction potential of the solids acting on a N-component fluid mixture in a porous medium, we postulate that the Helmholtz free energy density can be expressed as

$$\psi = \phi\psi_0 + \frac{\phi^2}{2}\sum_{i=1}^{N}\sum_{j=1}^{N}\kappa_{ij}\nabla c_i.\nabla c_j + \phi\,\rho\varphi_g + \phi\sum_{i=1}^{N} c_i\varphi_{s,i} \tag{2}$$

where $\psi_0(c_1,c_2,\ldots)$ is the homogeneous Helmholtz free energy density, defined in terms of energy per unit volume of void space. $c_1,c_2,\ldots, c_N$ are the molar concentrations of the components. The coefficients κ_{ij} are related to the correlation functions for molecular densities in pore space and the whole second term on the right-hand side represent macroscopic fluid-fluid interfacial effects. The last two terms of ψ include the external potential energy functions due to gravitational attraction φ_g and fluid-solid interaction potentials for each component $\varphi_{s,i}$. Based on the description of the free energy density in Eq. (2), we derive continuity and momentum balance equations for the multiphase mixture. We first develop the chemical potential and the stress tensor expressions that

drive the flow of multiphase mixtures to equilibrium in porous media. Minimization of the energy functional leads to the set of Euler-Lagrange equations for molar concentrations of the components, through which the chemical potential, Φ_i, for the *ith* component, equal to the variational derivative of E_H with respect of c_i, is expressed as

$$\begin{aligned} \Phi_i &= \frac{\partial \psi_0}{\partial c_i} - \phi \sum_{j=1}^{N} \kappa_{ij} \nabla^2 c_j + M_i \varphi_g + \varphi_{s,i}^* \\ \varphi_{s,i}^* &= \varphi_{s,i} + \sum_{j=1}^{N} c_j \frac{\partial \varphi_{s,j}}{\partial c_i} \end{aligned} \tag{3}$$

where M_i is the molecular mass of the *ith* component. Skipping the detailed derivations, we here present only the final equations used for analyzing the experimental for the two-component-two-phase system (water-air). The detailed derivations of the general model will be presented in a manuscript currently under development. For isothermal systems, the balance equations for molar concentration of the *two* components multiphase mixture can be expressed as

$$\begin{aligned} \frac{\partial (\phi c_1)}{\partial t} + \nabla . (\boldsymbol{q} c_1 + \boldsymbol{J}_1) = 0 \\ \frac{\partial (\phi c_2)}{\partial t} + \nabla . (\boldsymbol{q} c_2 + \boldsymbol{J}_2) = 0 \end{aligned} \tag{4}$$

where $\boldsymbol{q}$ is the mass averaged velocity of the multiphase mixture, and $\boldsymbol{J_i}$ is the diffusive flux vector for the component i. Neglecting the inertial forces in porous media, the momentum equation for the multiphase mixture in the new model is expressed as

$$0 = -\frac{\mu \boldsymbol{q}}{k} - \nabla p - \rho \nabla \varphi_g + \underbrace{\phi \kappa (c_1 + c_2) \nabla \left(\nabla^2 c_1 + \nabla^2 c_2 \right)}_{\text{fluid-fluid interfacial interactions}} - \underbrace{c_1 \nabla \varphi_{s,1}^* - c_2 \nabla \varphi_{s,2}^*}_{\text{fluid-solid interactions}} \tag{5}$$

where $\boldsymbol{q}$ (LT^{-1}) is the specific discharge or Darcy velocity vector of the multiphase fluid mixture, p ($ML^{-1}T^{-2}$) is the mixture pressure ($p = -\psi_0 + \sum_i c_i \partial \psi_0 / \partial c_i$), $\boldsymbol{k}$ (L^2) is the intrinsic permeability tensor, ϕ is the porosity, ρ (ML^{-3}) is the mixture density, and μ ($ML^{-1}T^{-1}$) is the effective viscosity of the multiphase mixture. As clearly seen, the first three terms resemble the classical Darcy equation for single phase flow. However, the proposed representation of the momentum balance is significantly different from the classical multiphase extension of the Darcy equation. Eq. (5) does not include relative permeability for different phases nor does it utilize a macroscopic capillary pressure-saturation function. Eq. (5) also does not include additional equations for interfacial area descriptions as in the more recent theories of continuum-scale multiphase theory (*Niessner et al.*, 2011). Instead, the last two terms in Eq. (5) explicitly account for the effects of multiphase potential fluid-fluid and fluid-solid interaction forces.

Consistent with the thermodynamic constraints, the diffusive fluxes of the components are represented by employing the Maxwell-Stefan diffusion approach, including Knudsen or matrix diffusivity contributions in low permeability media. The diffusive fluxes are obtained from the following two equations for two components as functions of chemical potential gradients and molar concentrations:

$$-\frac{x_1}{RT}\nabla\Phi_1 = \frac{x_2\boldsymbol{J}_1 - x_1\boldsymbol{J}_2}{c_t D_{12}} + \frac{\boldsymbol{J}_1}{c_t D_{1M}}$$
$$-\frac{x_2}{RT}\nabla\Phi_2 = \frac{x_1\boldsymbol{J}_2 - x_2\boldsymbol{J}_1}{c_t D_{12}} + \frac{\boldsymbol{J}_2}{c_t D_{2M}} \quad (6)$$

where x_1 and x_2 represent the mole fractions for the components. The effective binary molecular diffusion coefficients and matrix diffusivities under multiphase flow conditions for each component are computed using Vignes' approach, based on interpolation of the component diffusivities in liquid and gas phases[*Vignes*, 1966].

The solution of equations (4) - (6) represents the distribution of molar densities in porous media through which volumetric saturations of different fluids can be estimated as in the traditional approach. In this task, we developed a numerical model solving the resulting coupled fourth order partial differential equations for two components, based on the finite volume method.

To represent the Helmholtz free energy density, a quadratic equation similar to the one proposed by *Armstrong et al*. [2016] was employed under fixed temperature condition. The parameters of the energy density function were obtained by fitting it to the equation of state properties for air-water mixture under both liquid and gas conditions.

In order to characterize the fluid-solid interaction energy terms in the model, we employed simplified coarse-grained molecular dynamics simulations using our model based on MDPD approach. Figure 19 shows variations of fluid-solid interaction energy functions (normalized by the maximum value in the figure) as function of mol fraction. The figure was obtained for water-oil system, but similar computations could be done different multiphase systems. Based on our analyses, we represented the following fluid-solid interaction energy functions, in terms of energy per mole, appeared to fit the MDPD results:

$$\varphi_{s,1} = Ah_1 \exp\left[-x_1\left(a_1 + \beta_1 x_2\right)\right]$$
$$\varphi_{s,2} = Ah_2 \exp\left[-x_2\left(a_2 + \beta_2 x_1\right)\right] \quad (7)$$

where Ah, a and β are the empirical parameters that may vary depending on pore geometry, pore size distribution, fluid and solid molecule types.

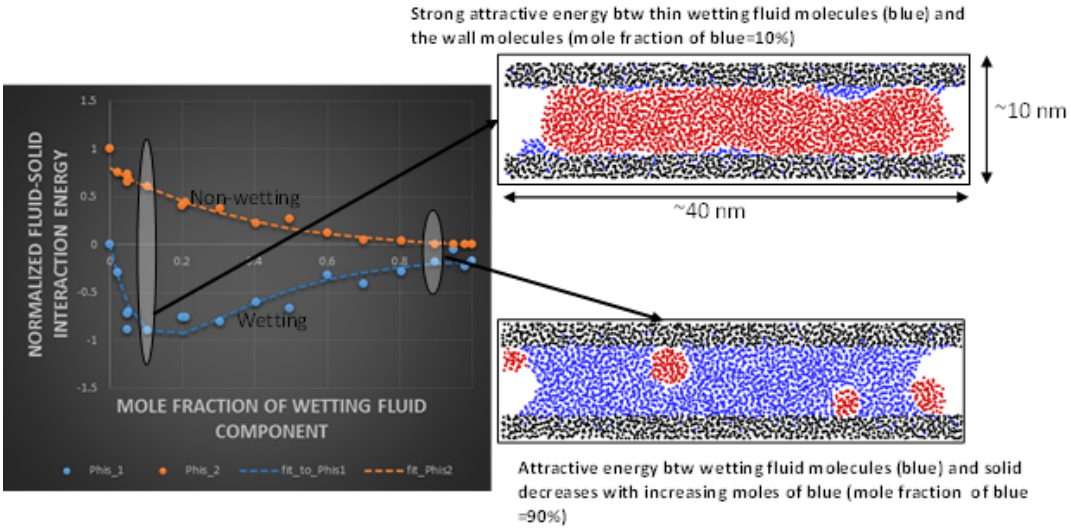

Figure 19. Preliminary demonstration of the MDPD (many-body dissipative particle dynamics) approach to characterize interaction energy functions as function of molar concentration in slit-shaped nanopores.

Application of the DFM Approach to Capillary Condensation in Shale

Because we recently completed the development of a numerical model, we present results only for one shale sample. However, the manuscript under development will present the results for all the shale sample experiments under high relative humidity conditions. As described in Task 2, the Marcellus shale samples equilibrated at RH = 0.31 was exposed to the RH = 0.81 condition. The experimental data indicated significant water uptake and long equilibration times. Although the enhanced water uptake could occur due to many different processes in the shale as described earlier, we focus here only on the multiphase flow physics aspect and investigate water uptake changes as a result of strong water-pore wall attraction in the nanopores of the shale. We present below the preliminary results of the model applied to the shale sample 7444, exposed to RH = 0.31 for about 21 days and then exposed to RH = 0.81 for additional 50 days. We simulate the experiments using a one-dimensional version of the model. The molar concentrations at the surfaces are fixed based on RH values. Also, for each relative humidity exposed at the surface, we fixed the strength of the fluid-solid interaction term at both boundaries.

Table 9 presents the estimated model parameter values by fitting the model to the water uptake data. Figure 20 shows that the model appears to represent the data very well, except the very early stage of RH=0.31 condition. The fitting shows that the permeability of the shale is extremely low and the matrix diffusivity terms appear to be also low compared to the simplified model analyzes in the first part of the task for Marcellus rock samples.

Figures 21a and 21b represent model calculated water molar concentration profiles in the shale core. The chemical potential gradients of the components result in water uptake into the rock. The model results suggest that the presence of strong fluid-solid interaction in the rock space could create enhanced water uptake at high RH and sustained disequilibrium for long time. However, these are preliminary analyses, and we are still at early stage to make definite conclusions. Detailed sensitivity analyzes to investigate the effect of different model parameters on the results will be presented in the manuscript under development. The model results appear to be promising for representing multiphase phenomena. However, further research and analyses are needed to test the model under broader conditions and apply the model at field scale for investigating various oil/gas recovery in unconventional reservoirs.

Table 9. Estimated DFM parameters for a Marcellus shale sample (Sample #7444) (parallel to lamination)

Permeability, k (m^2)	3.00×10^{-22}
Fluid-fluid interaction term, κ□(J L^2/mol^2)	3.52×10^{-7}
Component #1 (water)-solid interaction parameter Ah_1 (J/mol)	-1.73×10^{6}
a_1 (-)	1.90
β_1 (-)	1.26×10^{-4}
Matrix diffusivity term for component 1 (water molecules in liquid), D_{1M} (liq) (m^2/s)	4.48×10^{-12}
Matrix diffusivity term for component 1 (water molecules in gas phase), D_{1M} (g) (m^2/s)	1.00×10^{-9}
Component #2 (air)-solid interaction parameter, Ah_2 (J/mol)	583.42
a_2 (-)	-1.48
β_2 (-)	0.0
Matrix diffusivity term for component 2 (air molecules in liquid), D_{2M} (liq) (m^2/s)	3.59×10^{-12}
Matrix diffusivity term for component 2 (air molecules in gas phase), D_{2M} (g) (m^2/s)	8.02×10^{-10}
φ_{s1}* (J/mol) at boundaries (Rh=0.31)	-79.98×10^{2}
φ_{s1}* (J/mol) at boundaries (Rh=0.8)	-2.95×10^{2}

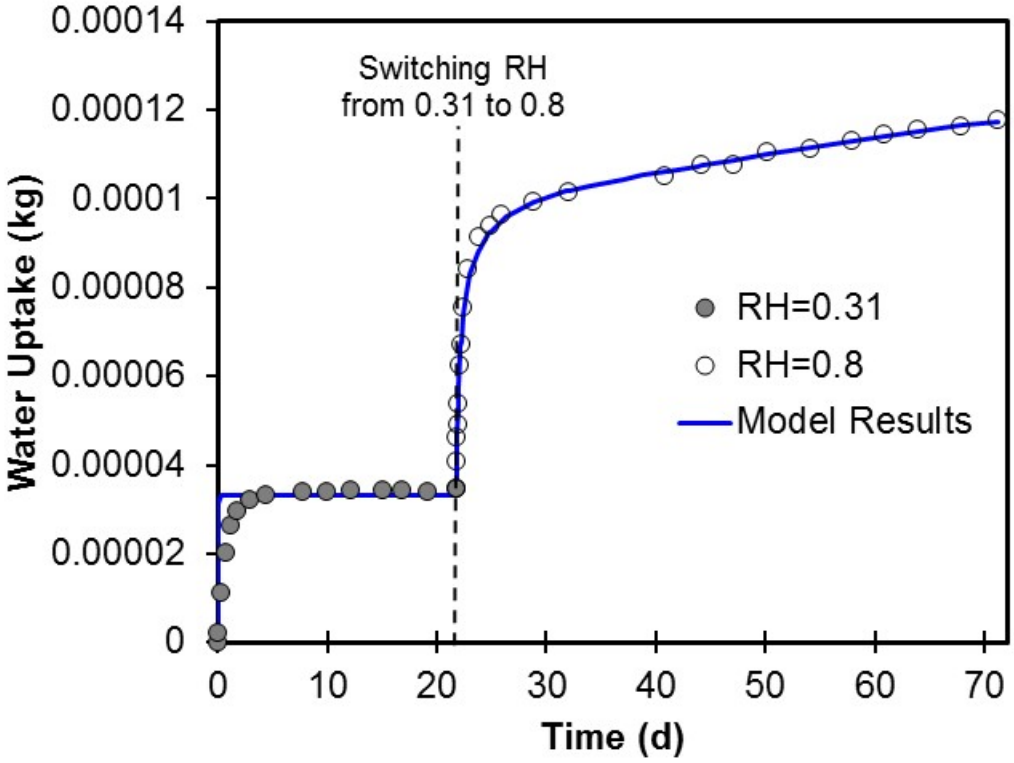

Figure 20. Comparisons of the model estimated and the measured water uptake in Marcellus shale.

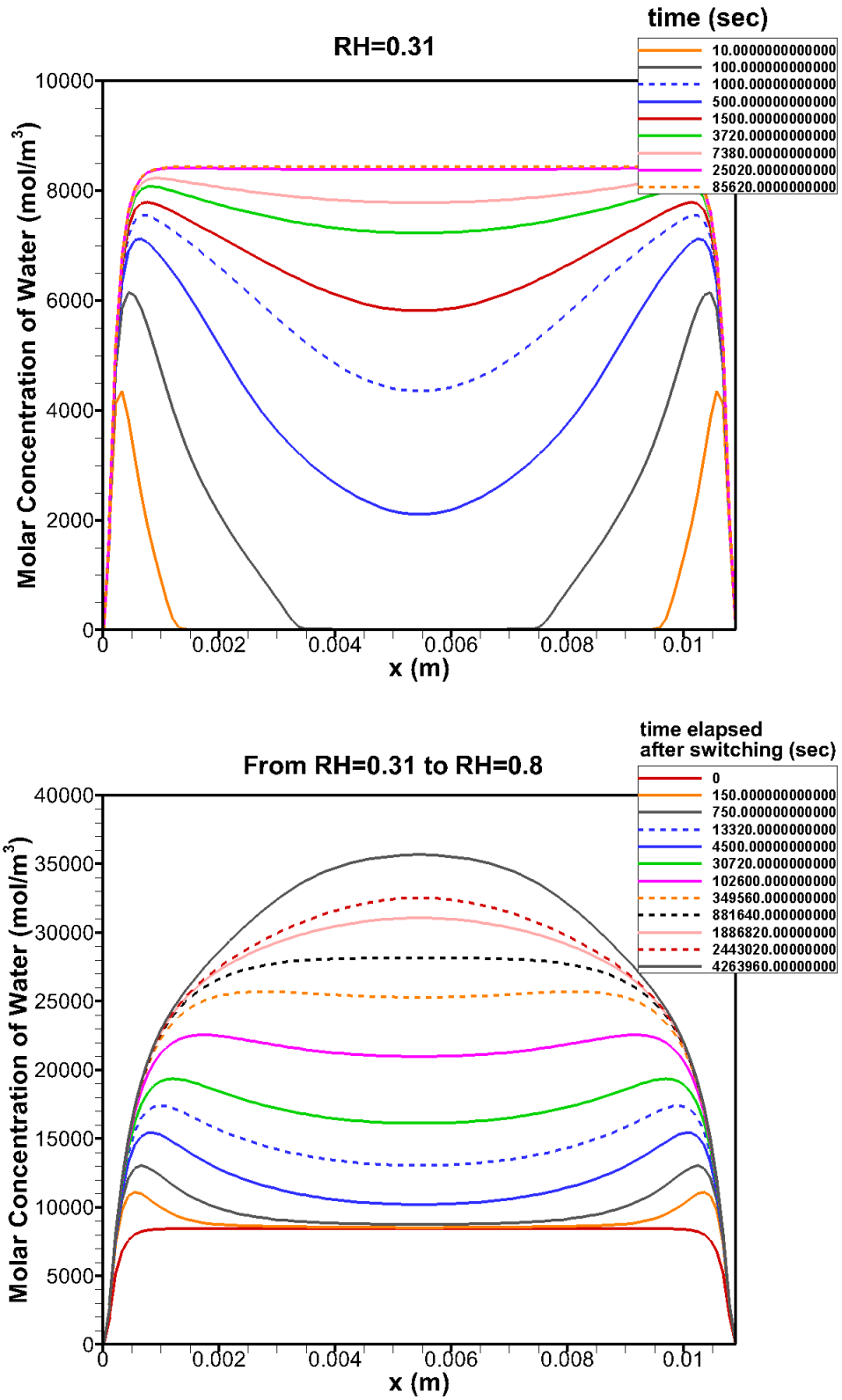

Figure 21. Molar concentration profile of water as a function of time in the shale rock sample at (**a**) RH=0.31 and (**b**) RH=0.81.

Task 4.B. Testing and development of macroscopic modeling approaches for flow processes of water and non-water fluids in shale matrix and across fracture-matrix interface:

The purpose of this subtask is to examine the potential influence of gravity segregation of injected fracturing fluid within the main hydrofracture and surrounding fracture network on gas productivity. The hypothesis being tested is that gravity drainage during and after reservoir stimulation leads to water accumulation in the lower part of the generated fractures (and potentially the associated stimulated reservoir volume), blocking the release of gas during the production phase. In addition, using a non-water fluid as alternative fracturing fluid is examined and compared to using slick water as fracturing fluid.

In the preparatory phase, we conducted simulations for a number of water imbibition experiments from three Woodford Shale samples (Table 1) including shale #3 from the Roetzal well (WR), shale # 5 from the Dunkin well (WD), and shale #7 from the Holt-1 well (WH1). The experiments were conducted under atmospheric pressure condition with a room temperature about 23 ˚C. Two experiments were conducted for each of the sample with different suction forces (40 mm suction and 3 or 2 mm suction) applied at one end of the core, where water enters the initially dry core. Details of experiments were provided in the final report for Phase 1 work.

TOUGH2 [*Pruess et al.*, 2012], a numerical simulator for non-isothermal flows of multicomponent, multiphase fluid in multi-dimensional porous and fractured media, was used to simulate the water imbibition process. iTOUGH2, a computer program that provides inverse modeling capabilities for the TOUGH2 code, was used to fit the observations from the experiments and estimate uncertain parameters of the samples [*Finsterle et al.*, 2017]. Microfractures were not considered in these initial models. The uncertain parameters for each core include: permeability (k), porosity (ϕ), residual liquid saturation (S_{lr}), residual gas saturation (S_{gr}), and two van Genuchten parameters used in the water retention curve: α – a parameter related to the inverse of the air entry pressure and n – a parameter related to pore size distribution. The observations from the experiments are the total water inflow over time. In addition to the estimation of the uncertain parameters, the analysis also provides the uncertainty range associated with each estimate, as well as the sensitivity of the model output (i.e., total water inflow) to the uncertain parameters.

Figure 22 shows both measured and simulated water inflow as a function of square root of time. The analysis show permeability k is the most influential parameters, followed by α and n in water retention curves. The other three parameters have very little sensitivity, their estimation uncertainties are large, which means their estimates are not very meaningful. Therefore, we only list the estimated permeability, α and n and their uncertainties in Table 10.

For each of the sample, the measure data from the two experiments show the water inflow is different with different suctions, which is not consistent with the simulation results. In the simulation the capillary pressure of the dry core is much larger than the suction applied, which diminishes the little difference between the two suction forces. As a result, the two curves for the two experiments almost fall on top of each other. The different water inflow for the two experiments observed in the measured data implies there might be microfractures that are responsible for the differences. The fractures are not included in the current numerical model.

For sample WD, as the two measured data sets are significant different, it is not possible to fit the two observation data sets with the same model parameters. The uncertainties for the estimated parameters are very large. The estimates should not be used for prediction.

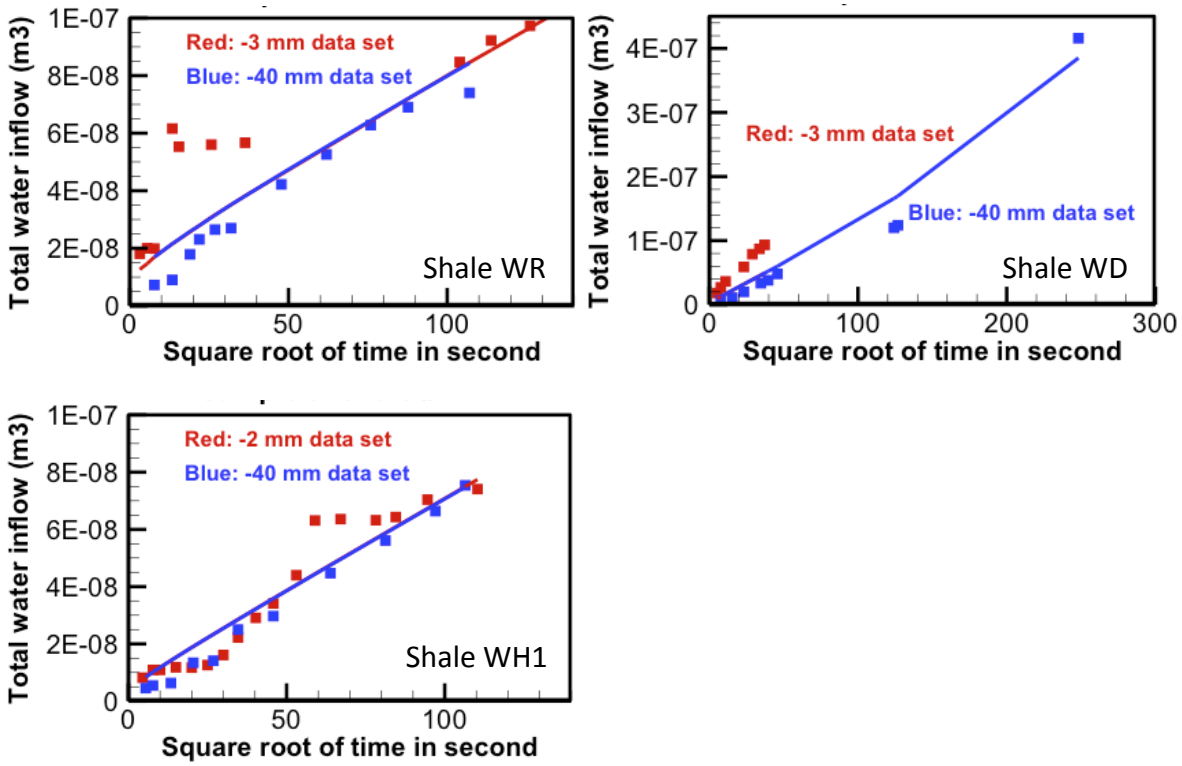

Figure 22. Final data fit for the two water imbibition tests for the three shale samples.

Parameter	Log10(k) (k in m^2)			Log(α) (α in Pa)			n		
Shale #	3	5	7	3	5	7	3	5	7
Shale	WR	WD	WH1	WR	WD	WH1	WR	WD	WH1
Estimation	-16.5	-15.5	-15.9	4.6	4.6	4.6	1.2	1.3	1.2
Uncertainty	1.0	4.4	0.5	0.8	5.2	0.7	0.75	4.3	0.4

Table 10. Estimated parameters and their uncertainties for the three shale samples.

To achieve the objective of evaluating fracture-matrix controls on gravity drainage, we performed the following activities: 1. conducted a literature survey; 2. performed simulations using a simple 2D model with one horizontal well, one vertical fracture and shale matrix in the system; 3. built a 3D multi-continuum model and performed simulations to study potential gravitational effects using water as injection fluid; and 4. performed simulations using alternative non-water fluid as stimulation fluid.

4.2.1 Literature review

A literature review was conducted to assess the current understanding of flow processes in shale matrix and across fracture-matrix interface. The main studies are summarized below:

- Liu et al. simulated the process of fracturing (fluid injection), shut-in and fracture closure (adjusting fracture permeability based on its relationship to stress change, adjust fracture volume/porosity/aperture based on cubic law), and production [*Liu et al.*, 2017]. They concluded: 1. Gravity segregation may lead to water accumulating at the bottom of a vertical planar fracture; however, fracture tortuosity could limit the segregation; 2. Extended shut-in time may result in an enhanced initial gas production but lower later-time production; 3. A uniform proppant distribution, which results in a uniform fracture permeability distribution, will lead to a higher cumulative gas production, whereas non-uniform proppant distribution may worsen the gravity segregation effect.
- Parmar et al. conducted laboratory experiments to investigate gravity effects [*Parmar et al.*, 2014]. The conclusion is that upward displacement of gas (water flowing against gravity) is unstable, leading to poor sweep efficiency. In addition, using surfactant (reduced capillary pressure) and changing the wettability of porous media from hydrophilic to hydrophobic will enhance water recovery.
- Agrawal and Sharma investigated factors that may influence productivity using numerical simulations [*Agrawal and Sharma*, 2013; 2015]. They concluded that low matrix permeability, low drawdown, high fracture permeability, and low fracture height are not favorable conditions to remove water from fractures. In their investigation, they changed one factor at a time, i.e., correlations between permeability and capillary pressure, fracture permeability and aperture (volume) are not considered.
- Tidwell and Parker conducted laboratory experiments and confirmed viscous fingering and gravity drainage effects on liquid displacement [*Tidwell and Parker*, 1996]. They also observed that as fluid viscosity decreases, vertical segregation due to gravity becomes more pronounced.
- Birdsell et al. focused their study on a dimensionless imbibition rate parameter (gravity is ignored), concluding that the intrinsic permeability of the shale and the viscosity of the fluids are the most important properties controlling the imbibition rate [*Birdsell et al.*, 2015].
- Sarkar et al. performed a number of numerical simulations to examine the impact of well placement [*Sarkar et al.*, 2016]. They concluded that upward vertical displacements, in which the fracturing fluid flows against gravity, results in the lowest recovery. In addition, the wettability of the rock matrix has a significant impact on ultimate recovery when the effect of gravity is dominant.

The literature survey shows a relatively consistent recognition that gravity plays a role in gas production, i.e., less of the injected fracturing water is produced from the lower part (lower than the horizontal well) of the fracture; as a result, the water that is not produced inhibits gas production in the long run. But it is not clear how strong the effect could be and how it is affected by various parameters.

4.2.2 Simple 2D Model

The first model used to examine gravity effects was a simple 2D model with a vertical fracture (perpendicular to the XZ plane in Figure 23) and a horizontal wellbore. The background pressure in the model was 150 bar. The fracture has an aperture of 1 mm and a permeability of 10 darcy. The shale matrix has a permeability of 5×10^{-18} m^2, and a porosity of 5%. Initially, water was injected for two hours to mimic the water injected during the fracking process. Figure 23a shows liquid saturation in the matrix before gas production starts. Figure 23b shows liquid saturation in the matrix after 100 days of gas production, suggesting that a significant amount of water below the well level was trapped in the matrix due to gravity effect. Figure 24 shows the gas production rate from both the upper and lower region (relative to well location) for the first 100 days. Initially, gas production appears to be insignificantly higher from the lower region (compared to the upper region) due to a slightly stronger gradient. At later times, gas production from the lower region decreases more strongly.

This simple model shows that more water is removed from the upper region during the initial production period. Due to gravity effects, a significant amount of water is left unproduced in the lower region; it imbibes into matrix, leading to smaller gas production compared to the upper region at later times.

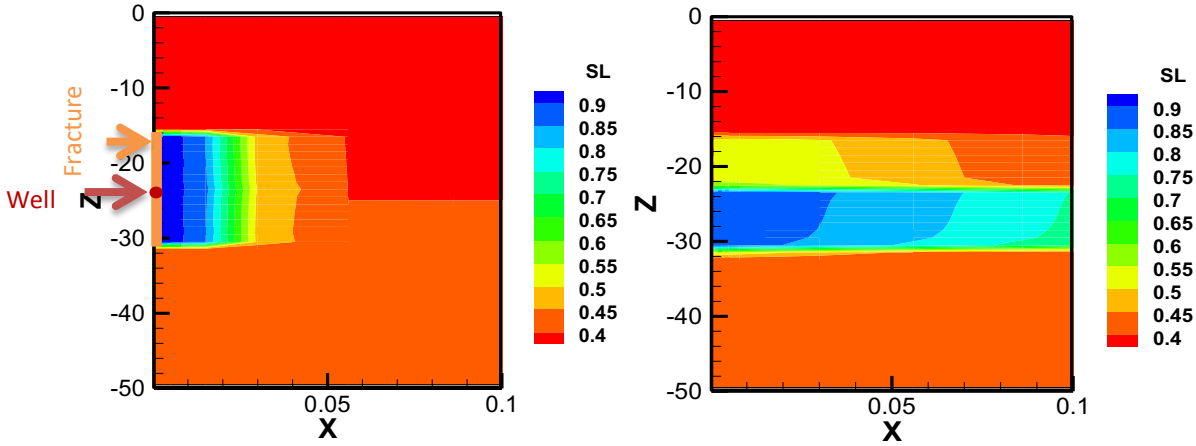

Figure 23. (**a**). Liquid saturation after two hours of water injection, used as initial condition for the subsequent production phase; (**b**). Liquid saturation after 100 days of production.

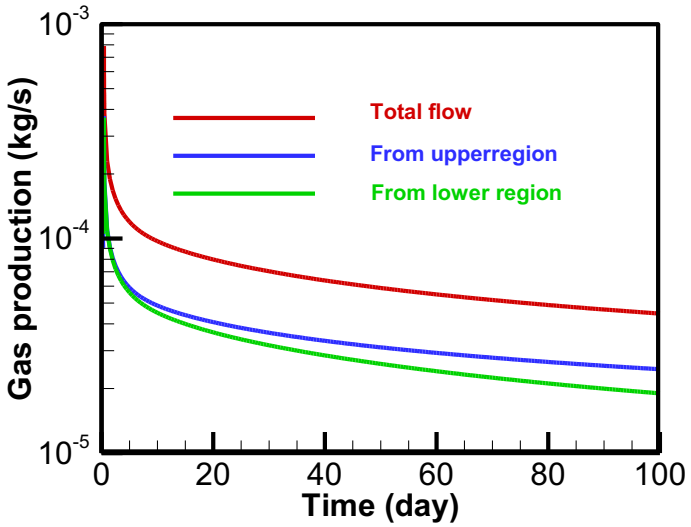

Figure 24. Total gas production rate and the respective contributions from the upper and lower regions.

4.2.3 3D Multi-Continuum Model

The significance of the gravitational effect appears to depend on the relative properties of the generated fracture, the stimulated fracture network, and the gas-bearing shale matrix. Various coupled processes contribute to this effect, including (1) fracture opening and associated permeability changes, (2) only partial closing of the stimulated fracture in the sheared or propped fractures during production, (3) imbibition of fracking fluid and associated water blocking, (4) potential clay swelling and osmotic effects, (5) capillarity and wetting properties, as well as (6) small- and intermediate-scale heterogeneity of the stimulated reservoir volume. To simulate these processes, a 3D multi-continuum model (shale matrix, hydrofrac and small-scale fracture network) was built. The mesh was generated using the MINC (multiple interacting continua) method in TOUGH2 [*Pruess et al.*, 2012].

In preparation for these analyses, the multi-phase, multicomponent simulator TOUGH2-EOS7C (Oldenburg et al., 2004), which is integrated in the iTOUGH2 simulation-optimization framework[*Finsterle et al.*, 2017], has been expanded to account for pressure-dependent permeabilities with the possibility of only partial fracture closure during production.

In this model, the 200 m thick reservoir has an initial hydrostatic pressure (with an average pressure of 30 MPa) and a uniform initial gas saturation of 75%; the gas phase consists of methane. The fracking fluid is slickwater; it contains a tracer for tracking its migration. However, the tracer has no impact on fluid properties.

A three-stage reference scenario has been defined, consisting of a two-hour fracking period, followed by a seven-day soaking (shut-in) period, before gas is produced against a constant wellbore pressure of 20 MPa.

During the fracking period, slickwater is injected at a constant rate from a horizontal well, which is perforated over a length of 6 m. At the location of the potential vertical hydrofrac, properties are defined such that permeability increases substantially (using a third-power law, see Table 1) as aperture increases in response to increased fluid pressure. As a constraint, the pressure in the

injection well is limited to a maximum value of 90 MPa. Once the maximum injection pressure is reached, operation is automatically switched from constant-rate to constant-pressure injection.

The region around the vertical hydrofrac and along the horizontal well (while initially homogeneous with the very low permeability of intact shale) is allowed to evolve into a dual-porosity fracture-matrix system, again with porosity and permeability of the fracture network dynamically calculated as a function of pore pressure. To accurately simulate the exchange of fracfluid and gas between the fracture network and the shale, each volume representing the matrix continuum is discretized into four grid blocks using the multiple interacting continua (MINC) approach. During the development of the hydrofrac and associate network of small fractures, capillary forces are dynamically adjusted as a function of permeability, aperture, and saturation. The potential impacts of turbulence during injection and production are accounted for using the Forchheimer equation [*Forchheimer*, 1901] with the non-Darcy flow coefficient calculated according to Geertsma [*Geertsma*, 1974].

Table 11 shows the property set used in the preliminary simulations discussed below. Initially, the entire model domain has the uniform hydraulic properties of intact shale. A higher pore compressibility is assigned to the potential location of the vertical hydrofrac and the fracture continuum in its immediate vicinity. As fracking fluid (here: slickwater) is injected, the pressure increases, leading to an increase in porosity (i.e., fracture aperture) and associated increase in permeability, dynamically creating the hydrofrac and the secondary network of small fractures. As the fracture apertures increase, their capillary strength is reduced according to the Leverett scaling rule. The properties of the shale matrix remain essentially constant.

Figure 25 illustrates the extent of the hydrofrac at the end of the two-hour stimulation period. Initial simulations of the subsequent, one-week long soaking period and five-year long production phase indicate that traces of fracking fluid may remain in the fractured system for an extended period.

Figure 26 qualitatively shows the concentration of fracking fluid in the pore water of the hydrofrac and the network of small fractures. Note that while the hydrofrac is fully liquid saturated after fracking, liquid saturations at the end of the soaking and production phases are near residual values, as fracfluid is imbibed into the fracture network and from there into the shale matrix, initially driven by the high injection pressure, and later by the strong capillary suction of the low-saturation shale matrix.

This is illustrated in Figure 27, which shows the liquid saturation after fracking, soaking and production. The initial liquid saturation in this gas reservoir is 25% throughout the model domain. Figure 27 also suggests that for the chosen property set (specifically the strong capillarity of the shale matrix), gravity drainage in the hydrofrac is a very small effect, because the fracfluid is preferentially being sucked into the small fractures and the matrix. The saturation in the hydrofrac quickly approaches residual values with very small relative permeability, making gravity flow a minor contributor for fluid redistribution.

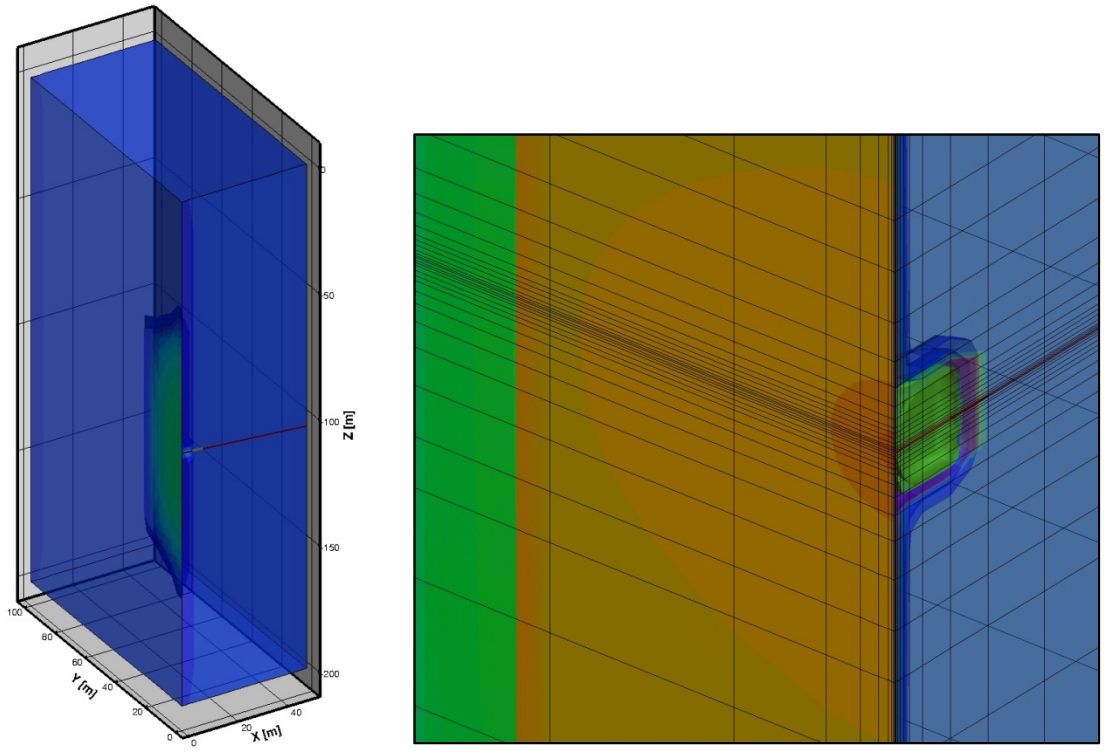

(**a**) (**b**)

Figure 25: Discrete, vertical hydrofrac, surrounded by stimulated network of smaller fractures represented by a dual-continuum model at the end of the two-hour injection period; (**a**) aperture distribution in entire model domain, (**b**) close-up of permeability structure near perforated well section.

Table 11: Material properties

Parameter	Units	Value
Shale matrix		
absolute permeability, k	m^2	10^{-18}
porosity, ϕ	%	5.0
pore compressibility expansion, c_{ϕ}	Pa^{-1}	10^{-9}
pore compressibility contraction, $c_{\phi con}$	Pa^{-1}	10^{-9}
residual liquid saturation, S_{lr}	%	20.0
residual gas saturation, S_{gr}	%	0.0
van Genuchten pore-size distribution index, n	-	2.0
van Genuchten capillary strength, α	Pa^{-1}	10^{-6}
Hydrofrac		
initial absolute permeability, k_0	m^2	10^{-18}
porosity-dependent absolute permeability, k	m^2	$k(\phi) = k_0 \left(\frac{\phi}{\phi_0}\right)^B$
exponent, B	-	3.0
maximum absolute permeability, k_{max}	m^2	10^{-11}
initial porosity, ϕ_0	%	5.0
pressure-dependent porosity, ϕ	%	$\phi = \phi_0 e^{-c_\phi \Delta P}$
pore compressibility, c_{ϕ}	Pa^{-1}	10^{-7}
pore compressibility contraction, $c_{\phi con}$	Pa^{-1}	10^{-9}
residual liquid saturation, S_{lr}	%	20.0
residual gas saturation, S_{gr}	%	0.0
van Genuchten pore-size distribution index, n	-	2.0
reference van Genuchten capillary strength, α_0	Pa^{-1}	10^{-6}
van Genuchten capillary strength, $\alpha(k,\phi)$	Pa^{-1}	$\alpha = \alpha_0 \sqrt{\frac{k_0 \cdot \phi}{k \cdot \phi_0}}$
Small-scale fracture network		
initial absolute permeability, k_0	m^2	10^{-18}
porosity-dependent absolute permeability, k	m^2	$k(\phi) = k_0 \left(\frac{\phi}{\phi_0}\right)^B$
exponent, B	-	3.0
maximum absolute permeability, k_{max}	m^2	10^{-14}
initial porosity, ϕ_0	%	5.0
pressure-dependent porosity, ϕ	%	$\phi = \phi_0 e^{-c_\phi \Delta P}$
pore compressibility, c_{ϕ}	Pa^{-1}	5×10^{-8}
pore compressibility contraction, $c_{\phi con}$	Pa^{-1}	10^{-9}
residual liquid saturation, S_{lr}	%	20.0
residual gas saturation, S_{gr}	%	0.0
van Genuchten pore-size distribution index, n	-	2.0
reference van Genuchten capillary strength, α_0	Pa^{-1}	10^{-6}
van Genuchten capillary strength, $\alpha(k,\phi)$	Pa^{-1}	$\alpha = \alpha_0 \sqrt{\frac{k_0 \cdot \phi}{k \cdot \phi_0}}$
fracture spacing (3 orthogonal sets)	m	1.0

Figure 28 confirms that imbibition of fracfluid into the shale matrix is substantial. Despite the stimulation, the total volume of the fractures is relatively small. However, in this gas reservoir, there is sufficient space in the gas-filled shale pore space to accommodate most of the fracking fluid, which is absorbed by strong capillary forces. Once in the low-permeable matrix, the fracfluid is difficult to remove, even during an extended production period, which has a negative impact on gas production.

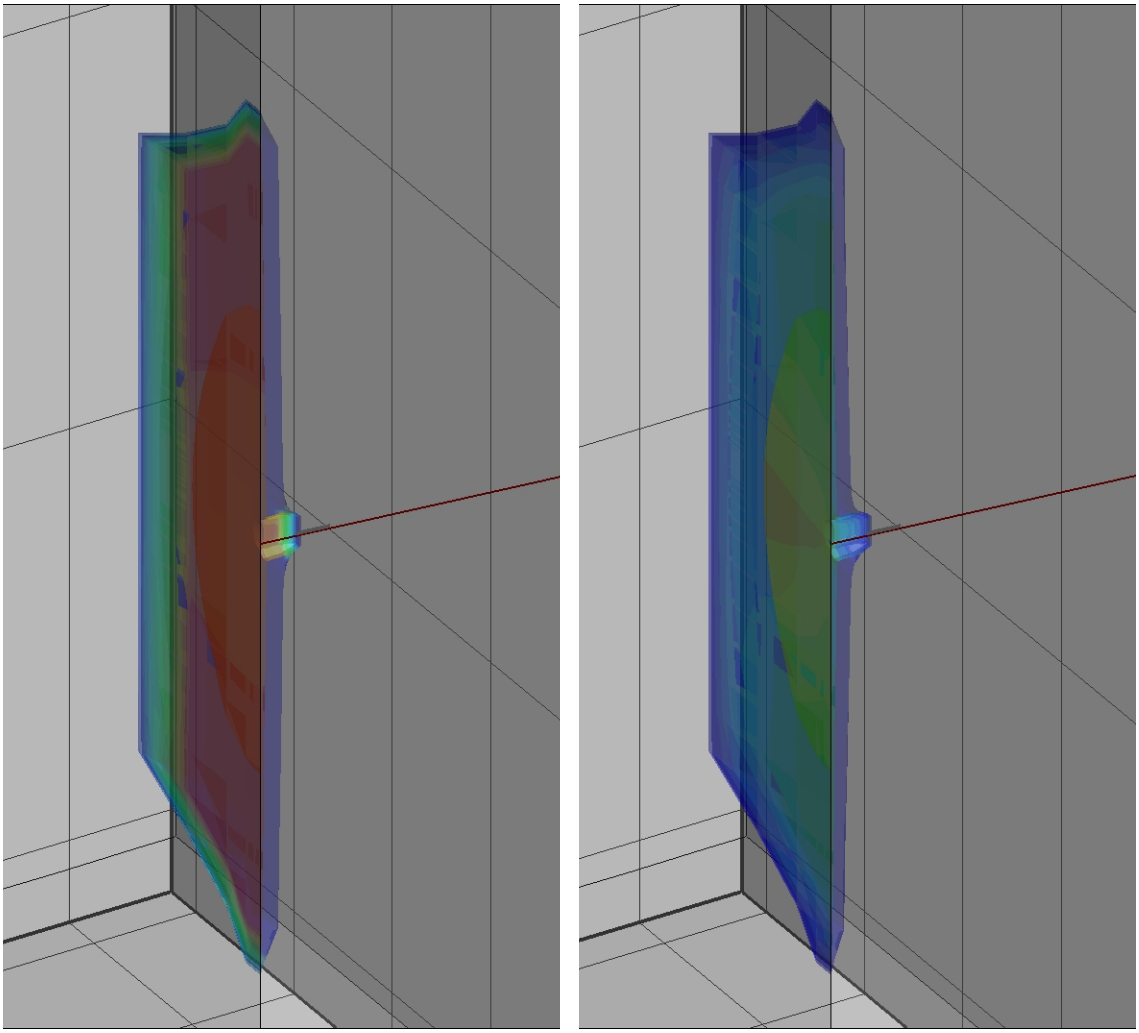

(**a**) (**b**)

Figure 26: Concentration of fracking fluid in pore water after (**a**) one week of soaking (shut-in), (**b**) five years of production.

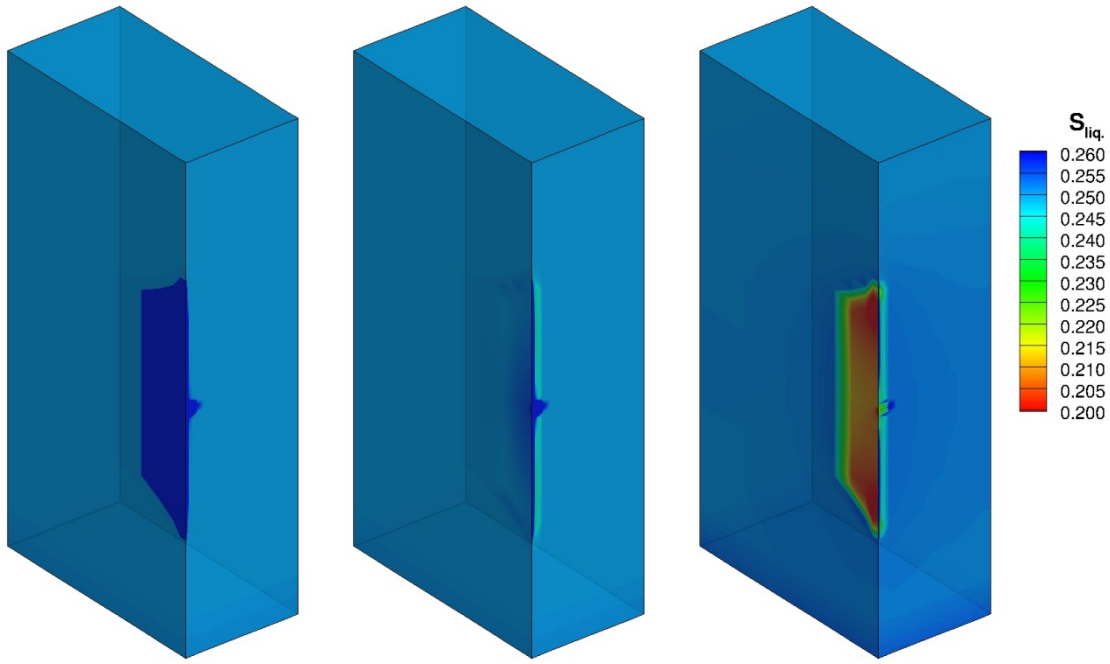

(**a**) (**b**) (**c**)

Figure 27: Liquid saturation after (**a**) fracking, (**b**) soaking, and (**c**) production.

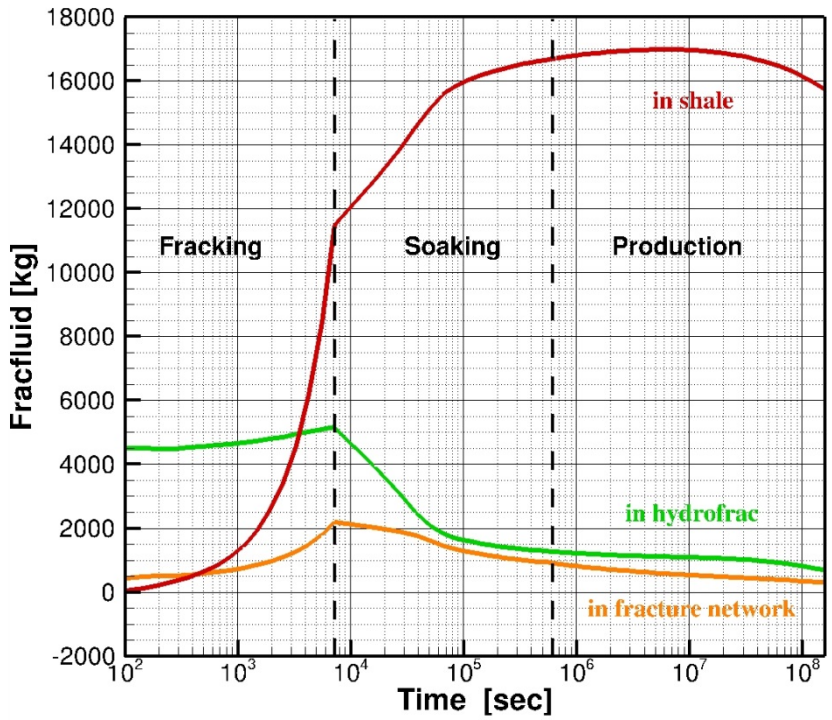

Figure 28: Distribution of injected fracking fluid among hydrofrac, network of small fractures, and shale matrix as a function of time during the fracking, soaking, and production stages.

The network of small fractures in the 3D model, which is not present in the 2D model, has the effect of greatly increasing access of fracfluid to the matrix. As a result, the fracture network substantially increases water imbibition into the shale, lowering liquid saturation in the main hydrofrac and thus reducing the associated gravity-drainage effects.

4.2.4 Using CO_2 as Fracturing Fluid

Using the same multi-continuum model, CO_2 was investigated as an alternative non-water fracking fluid (the injected fluid is changed to CO_2). Figure 29 shows the distribution of injected CO_2 among hydrofrac, network of small fractures, and shale matrix as a function of time during the fracking, soaking, and production stages. A constant pressure is applied to both water and CO_2 injection. Compared to water, the injected CO_2 mass is about half of the injected water. If using water as the fracking fluid, the strong capillary pressure from the matrix provides an additional driving force for water imbibition; this effect is much reduced or absent when using CO_2 as the fracking fluid. During the production period, most of the injected CO_2 is retrieved, while the majority of the injected slick water remains in the matrix, held by capillary pressure. Only a portion of the water in the hydrofrac and fracture network is produced back.

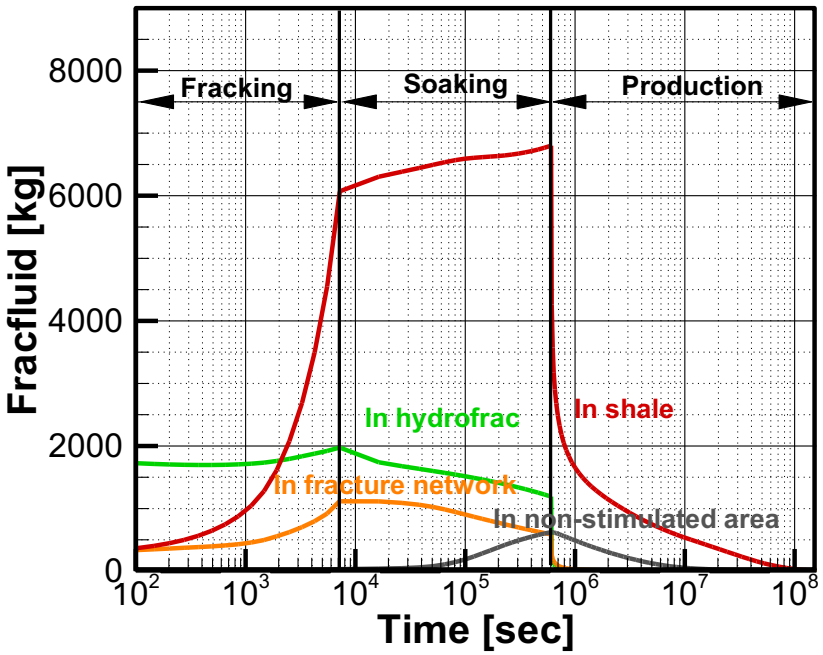

Figure 29. Distribution of injected CO_2 among hydrofrac, network of small fractures, and shale matrix as a function of time during the fracking, soaking, and production stages.

4.2.5 Conclusion

The goal of this subtask is to understand if and how much gravity segregation could affect gas production in a horizontal well setup scenario using water as fracking fluid, and how it could be different if an alternative non-water fluid had been used. Two simulations were performed, one of a system with one main vertical hydrofrac embedded in the gas-bearing shale matrix (i.e., the 2D

simple model) and a second, 3D model, which includes the main hydrofrac, and a network of small fractures surrounding the hydrofrac; both the large hydrofrac and the network of smaller fractures are connected to the shale matrix. The simulations show that the inclusion of the network of small fractures increases the imbibed liquid volume for both the upper and lower sections of the hydrofrac. As a result, gravitational effects are not apparent as they are in the model without a network of small fractures. The message from the study is that the gravity segregation effect depends on the actual geological system. For a system with only a few large hydrofracs, gravity effects may play a role (as also demonstrated by other modeling studies), whereas increased fracfluid imbibition promoted by formation damage around the main hydrofrac drastically reduces water saturation in the fractures and associated gravity effects. Nevertheless, imbibition into the shale matrix may lead to water blocking and thus reduced gas production.

Acknowledgments
Support for this research provided by DOE-NETL, and project management by Stephen Henry (NETL) are gratefully acknowledged. We thank Yongman Kim and Weijun Shen for their laboratory efforts at the beginning of the project, and the MSEEL and Oklahoma Geological Survey for shale samples.

References

Agrawal, S., and M. M. Sharma (2013), Impact of liquid loading in hydraulic fractures on well productivity, in *SPE Hydraulic Fracturing Technology Conference*, edited, p. 16, Society of Petroleum Engineers, The Woodlands, TX.

Agrawal, S., and M. M. Sharma (2015), Practical insights into liquid loading within hydraulic fractures and potential unconventional gas reservoir optimization strategies, *Journal of Unconventional Oil and Gas Resources*, *11*, 60-74.

Armstrong, R. T., S. Berg, O. Dinariev, N. Evseev, D. Klemin, D. Koroteev, and S. Safonov (2016), Modeling of Pore-Scale Two-Phase Phenomena Using Density Functional Hydrodynamics, *Transport in Porous Media*, *112*(3), 577-607.

Birdsell, D. T., H. Rajaram, and G. Lackey (2015), Imbibition of hydraulic fracturing fluids into partially saturated shale, *Water Resour. Res.*, *51*(8), 6787-6796.

Borek, S. L. (1994), Effect of humidity on pyrite oxidation, *Acs Sym Ser*, *550*, 31-44.

Busch, A., and A. Amann-Hildenbrand (2013), Predicting capillarity of mudrocks, *Mar Petrol Geol*, *45*, 208-223.

Cahn, J. W., and J. E. Hilliard (1958), Free Energy of a Nonuniform System .1. Interfacial Free Energy, *J. Chem. Phys.*, *28*(2), 258-267.

Cardott, B. J. (2012), Thermal maturity of Woodford Shale gas and oil plays, Oklahoma, USA, *International Journal of Coal Geology*, *103*, 109-119.

Crank, J. (1975), *The Mathematics of Diffusion*, second ed., 415 pp., Clarendon, Oxford.

Dane, J. H., and J. W. Hopmans (2002), Pressure plate extractor, in *Methods of Soil Analysis, Part 4, Physical Methods*, edited by J. H. Dane and G. C. Topp, pp. 688-690, Soil Science Society America, Madison, WI.

Dinariev, O. Y., and N. V. Evseev (2017), Modeling of nanoscale liquid mixture transport by density functional hydrodynamics, *Phys. Rev. E*, *95*(6).

Dinariyev, O. Y. (1995), A hydrodynamic description of a multicomponent multiphase mixture in narrow pores and thin layers, *Pmm-J Appl Math Mec+*, *59*(5), 745-752.

Elgmati, M., H. Zhang, B. Bai, R. Flori, and Q. Qu (2011), Submicron-pore characterization of shale gas plays, in *SPE North American Unconventional Gas Conference and Exhibition*, edited, p. 19, Society of Petroleum Engineers, The Woodlands, Texas.
Finsterle, S., et al. (2017), iTOUGH2: A multiphysics simulation-optimization framework for analyzing subsurface systems, *Comput Geosci-Uk*, *108*, 8-20.
Forchheimer, P. (1901), Water movement through the ground., *Z Ver Dtsch Ing*, *45*, 1781-1788.
Freyer, D., and W. Voigt (2003), Crystallization and phase stability of CaSO4 and CaSO4-based salts, *Monatsh. Chem.*, *134*(5), 693-719.
Geertsma, J. (1974), Estimating coefficient of inertial resistance in fluid- flow through porous media, *Soc Petrol Eng J*, *14*(5), 445-450.
Greenspan, L. (1977), Humidity fixed-points of binary saturated aqueous solutions, *Journal of Research of the National Bureau of Standards Section A-Physics and Chemistry*, *81*(1), 89-96.
Gupta, D. V. S. (2009), Unconventional fracturing fluids for tight gas reservoirs, in *SPE Hydraulic Fracturing Technology Conference*, edited, p. 9, Society of Petroleum Engineers, The Woodlands, Texas.
Hohenberg, P., and W. Kohn (1964), Inhomogeneous Electron Gas, *Phys Rev B*, *136*(3b), B864-+.
Hoover, S. E., W. Greenawalt, and B. Tittmann (2015), Experimental and theoretical modeling of expansion in pyritic shale, *Geothechnical Testing Journal*, *38*(2), 166-178.
Huggins, F. E., G. P. Huffman, and M. C. Lin (1983), Observations on low-temperature oxidation of minerals in bituminous coal, *International Journal of Coal Geology*, *3*(2), 157-182.
Hutchins, R. D., and M. J. Miller (2005), A circulating-foam loop for evaluating foam at conditions of use, *SPE Production and Facilities*, *2005*(SPE 80242), 286-294.
Jerz, J. K., and J. D. Rimstidt (2004), Pyrite oxidation in moist air, *Geochim. Cosmochim. Acta*, *68*(4), 701-714.
Kohn, W. (1999), Nobel Lecture: Electronic structure of matter-wave functions and density functionals, *Rev Mod Phys*, *71*(5), 1253-1266.
Krishna, R., and J. A. Wesselingh (1997), Review article number 50 - The Maxwell-Stefan approach to mass transfer, *Chem. Eng. Sci.*, *52*(6), 861-911.
Li, J. R., R. J. Kuppler, and H. C. Zhou (2009), Selective gas adsorption and separation in metal-organic frameworks, *Chem. Soc. Rev.*, *38*(5), 1477-1504.
Liu, Y., J. Y. Leung, R. Chalaturnyk, and C. J. J. Virues (2017), Fracture fluid distribution in shale gas reservoirs due to fracture closure, proppant distribution, and gravity segregation, in *SPE Unconventional Resources Conference*, edited, p. 21, Society of Petroleum Engineers, Calgary, Alberta, Canada.
Loeb, L. B. (1961), *The Kinetic Theory of Gases*, 3rd ed., Dover Publications, Inc., New York.
Mason, G., and N. R. Morrow (2013), Developments in spontaneous imbibition and possibilities for future work, *Journal of Petroleum Science and Engineering*, *110*, 268-293.
Massman, W. J. (1998), A review of the molecular diffusivities of H2O, CO2, CH4, CO, O-3, SO2, NH3, N2O, NO, AND NO2 in air, O-2 AND N-2 near STP, *Atmos. Environ.*, *32*(6), 1111-1127.
Montgomery, C. (2013), Fracturing fluid components, in *Effective and Sustainable Hydraulic Fracturing*, edited by A. P. Bunger, et al., pp. 25-45, InTech, Rijeka, Croatia.
Morrow, N. R. (1990), Wettability and Its effect on oil-recovery, *Journal of Petroleum Technology*, *42*(12), 1476-1484.

Ozisik, M. N. (1980), *Heat Conduction*, John Wiley, New York.
Parmar, J., H. Dehghanpour, and E. Kuru (2014), Displacement of water by gas in propped fractures: Combined effects of gravity, surface tension, and wettability, *Journal of Unconventional Oil and Gas Resources*, *5*, 10-21.
Peng, S., Q. H. Hu, and S. Hamamoto (2012), Diffusivity of rocks: Gas diffusion measurements and correlation to porosity and pore size distribution, *Water Resour. Res.*, *48*.
Pollard, W. G., and R. D. Present (1948), On gaseous self-diffusion in long capillary tubes, *Physical Review*, *73*(7), 762-774.
Pruess, K., C. Oldenburg, and G. Moridis (2012), TOUGH2 User's Guide, Version 2, 197 pp, Lawrence Berkeley National Laboratory, Berkeley, CA.
Rowlinson, J. S., and B. Widom (1982), *Molecular Theory of Capillarity*, 327 pp., Clarendon Press, Oxford.
Roychaudhuri, B., T. T. Tsotsis, and K. Jessen (2013), An experimental investigation of spontaneous imbibition in gas shales, *Journal of Petroleum Science and Engineering*, *111*, 87-97.
Sarkar, S., M. Haghighi, M. Sayyafzadeh, D. Cooke, K. Pokalai, and F. M. Ali Sahib (2016), A Cooper Basin simulation study of flow-back after hydraulic fracturing in tight gas wells, *APPEA Journal*, *2016*, 369-392.
Schmid, K. S., and S. Geiger (2013), Universal scaling of spontaneous imbibition for arbitrary petrophysical properties: Water-wet and mixed-wet states and Handy's conjecture, *Journal of Petroleum Science and Engineering*, *101*, 44-61.
Seemann, T., P. Bertier, B. M. Krooss, and H. Stanjek (2017), Water vapor sorption on mudrocks, in *Geomechanical and Petrophysical Properties of Mudrocks*, edited by E. H. Rutter, et al., p. 33, Geological Society of London, London.
Shanley, K. W., R. M. Cluff, and J. W. Robinson (2004), Factors controlling prolific gas production from low-permeability sandstone reservoirs: Implications for resource assessment, prospect development, and risk analysis, *Aapg Bulletin*, *88*(8), 1083-1121.
Shaoul, J., L. van Zelm, and C. J. de Pater (2011), Damage mechanisms in unconventional-gas-well stimulation-A new look at an old problem, *Spe Prod Oper*, *26*(4), 388-400.
Tidwell, V., and M. Parker (1996), Laboratory imaging of stimulation fluid displacement from hydraulic fractures, in *SPE Annual Technical Conference and Exhibition*, edited by S. o. P. Engineers, pp. 793-804, Society of Petroleum Engineers, Denver, Colorado, USA.
Tokunaga, T. K. (1985), Porous media gas diffusivity from a free-path distribution model, *J. Chem. Phys.*, *82*(11), 5298-5299.
Tokunaga, T. K., W. J. Shen, J. M. Wan, Y. Kim, A. Cihan, Y. Q. Zhang, and S. Finsterle (2017), Water saturation relations and their diffusion-limited equilibration in gas shale: Implications for gas flow in unconventional reservoirs, *Water Resour. Res.*, *53*(11), 9757-9770.
van der Waals, J. D. (1894), Thermodynamische Theorie der Kapillarität unter voraussetzung stetiger Dichteänderung, *Z. Phys. Chem.*, *13*, 657.
Vignes, A. (1966), Diffusion in Binary Solutions - Variation of Diffusion Coefficient with Composition, *Ind Eng Chem Fund*, *5*(2), 189-&.
Wan, J. M., T. K. Tokunaga, W. M. Dong, and Y. Kim (2017), Extracting natural biosurfactants from humus deposits for subsurface engineering applications, *Energy & Fuels*, *31*(11), 11902-11910.
Wang, L., J. Wan, T. K. Tokunaga, Y. Kim, and Q. Yu (2018), Experimental and modeling study of methane adsorption onto partially saturated shales, *Water Resour. Res.*, *54*.

Wesselingh, J. A., and R. Krishna (2000), *Mass Transfer in Multicomponent Mixtures*, VSSD, Delft.
Xue, Z., et al. (2016), Ultradry carbon dioxide-in-water foams with viscoelastic aqueous phases, *Langmuir*, *32*(1), 28-37.